The Ground-Based Scanning Radiometer: A Powerful Tool for Study of the Arctic Atmosphere

Domenico Cimini, Ed R. Westwater, *Fellow, IEEE*, Albin J. Gasiewski, *Fellow, IEEE*, Marian Klein, *Member, IEEE*, Vladimir Ye. Leuski, and Sally G. Dowlatshahi

Abstract—Measurements of water vapor and clouds in the polar regions are difficult, because conventional instruments show little sensitivity ($\sim$1.3 K/mm) to low amounts. On the other hand, millimeter- and submillimeter-wavelength radiometry offers greatly enhanced sensitivity (up to 51.4 K/mm, depending upon frequency). For this reason, the National Oceanic and Atmospheric Administration's Physical Science Division designed a new instrument, the Ground-Based Scanning Radiometer (GSR), for continuous and unattended observations at millimeter and submillimeter wavelengths (50–380 GHz). The GSR was deployed for the first time during the Arctic winter radiometric experiment in March–April 2004. In this paper, we discuss the GSR calibration procedure, which allows for accurate measurements during clear and cloudy skies. Error-budget analysis and comparison with independent measurements show an absolute accuracy on the order of 1–2 K. Examples of multifrequency and multiangle GSR observations are illustrated, representing a valuable new data set for the study of water vapor, clouds, and atmospheric absorption models in the Arctic.

Index Terms—Arctic atmosphere, ground-based remote sensing, radiometry, water vapor.

I. INTRODUCTION

THE STUDY of the polar atmosphere is extremely important for understanding the climate of our planet. In fact, water vapor and clouds in the Arctic play a key role in controlling the Earth's climate, through greenhouse trapping of radiation and the feedback on global ice-coverage and sea-surface temperature [8]. Therefore, accurate measurements of the atmospheric water-vapor and cloud properties in the Arctic are essential for the improvement in modeling the energy budget of the Earth system.

Although the polar regions are frequently covered by satellite overpasses, the temporal (hours to days) and spatial (order of kilometers) resolutions provided by satellite-based remote sensing are rather coarse for microphysical studies. On the other hand, ground-based remote sensors provide continuous and accurate monitoring of the atmosphere microphysics on a local scale [29]. For example, hydrometer characteristics can be defined with greater confidence with surface-based sensors compared to current satellite instruments [35].

In spite of this need, there is a lack of continuous measurements in the polar region due to the extreme and remote conditions, leading to great uncertainty in the radiative properties of the Arctic atmosphere [33]. In addition, measurements of atmospheric integrated water vapor (IWV) and liquid water path (LWP) during cold and dry conditions are very difficult, because conventional instruments show little sensitivity to such low amounts [23]. Therefore, the accuracy of existing instrumentation is limiting the development of theory and modeling for the radiative process of the atmosphere.

For this reason, the Microwave System Development Branch of the National Atmospheric and Oceanic Administration's Physical Science Division (NOAA/PSD) developed a new instrument called the Ground-Based Scanning Radiometer (GSR). The GSR is based on an original design [17], which takes advantage of the experience collected from previous Arctic experiments [32] and from the development of NOAA aircraft instrumentation [11]. The GSR provides features that are very appealing for atmospheric research in very dry and cold environments, such as the poles and high-altitude regions. The main characteristics are the following.

1) Observations at 26 channels, from microwave to infrared wavelengths, including millimeter and submillimeter channels that are very sensitive to low contents of vapor and liquid water.
2) Observations at multiple elevation angles (continuous scan from $15°$ to $165°$).
3) Three stages of calibration for accurate measurements during clear and cloudy conditions.
4) Information on cloud depolarizations (four polarimetric channels).
5) Capability of simultaneously monitoring the main thermodynamic properties of the atmosphere (temperature, humidity, and liquid water).

The GSR was deployed for the first time during the Arctic Winter Radiometric Experiment 2004 [34]. The major goal was to demonstrate that millimeter-wave radiometers could substantially improve observations of low vapor and liquid water. Secondary goals included the demonstration of recently developed calibration techniques and the study of atmospheric
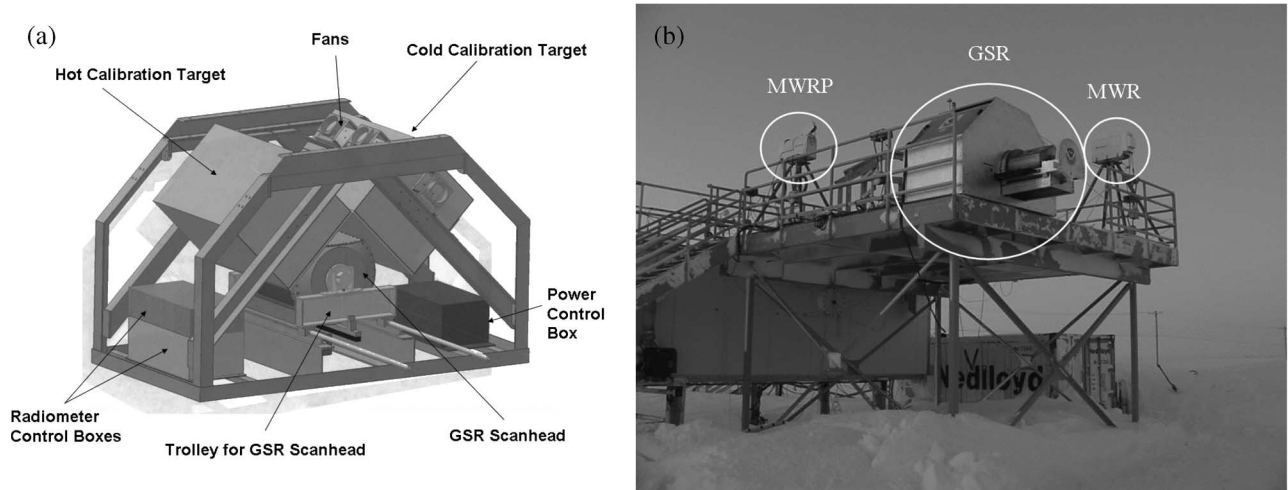
Fig. 1. (Left) Diagram of the GSR without its protective cover. (Right) Picture during the deployment at the ARM site in Barrow, AK.

absorption models over a broad frequency range. The ultimate purpose of the GSR deployment was to measure temperature, water vapor, and cloud properties, at cold ($-20\,°C$ to $-55\,°C$) and dry (IWV < 5 mm) conditions.

In this paper, we first illustrate the GSR design (Section II) and the experimental setup during the first deployment (Section III). In Section IV, we focus on details of the GSR calibration procedure, while in Section V, we compare GSR data with measurements from independent remote and *in situ* sensors. Finally, in Section VI, we summarize the achievements and discuss plans for future work.

II. SYSTEM DESIGN

The GSR system is depicted without its protective cover in Fig. 1(a). The core of the GSR consists of a cylindrical metal drum (called scanhead), which is able to spin $360°$ around its axis. The scanhead is mounted on a sliding trolley that can be moved in and out of the main housing. Inside the housing are located the boxes for radiometer and power control (bottom) and two external targets for calibration purposes (top). A picture of the GSR during the first deployment is shown in Fig. 1(b). The whole system is enclosed in a protective cover, leaving clearance for the scanhead to come out of the housing on the sliding trolley.

A. Scanhead

The scanhead contains six independent radiometers, receiving radiation through separate lens antennas located on the same plate, as pictured in Fig. 2. Thus, while the scanhead is rotating, all the antennas are pointing in the same direction, and the radiometers observe the same scene simultaneously. Each radiometer uses filter banks to split the radiation into different channels (as illustrated in Figs. 4 and 5), resulting in 11 channels in the 50–56-GHz region, two dual-polarization channels (H and V) at 89 GHz, seven channels around the 183.3-GHz water-vapor-absorption line, two dual-polarized channels at 340 GHz, and three channels around the strong water-vapor line at 380.2 GHz. Gaussian optics lens antennas [12] are used
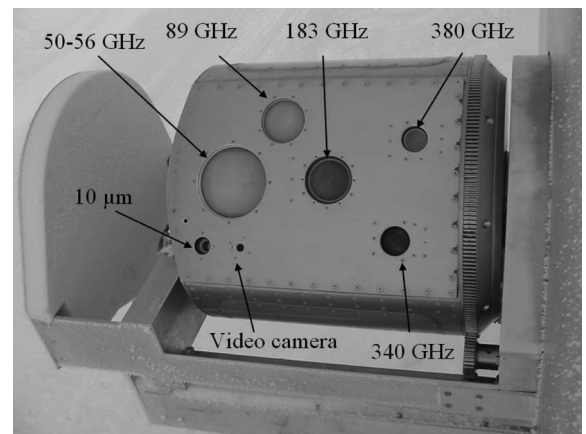

Fig. 2. Picture of the GSR scanhead with the lens antennas indicated for each radiometer. The lens antennas were designed to have approximately $3.5°$ beamwidth for 55- and 89-GHz radiometers and $1.8°$ for 183-, 340-, and 380-GHz radiometers.

to minimize the size of the horns; the diameters were chosen to have approximately $3.5°$ beamwidth (full-width at half-maximum) for the first two radiometers (50–89 GHz), while $1.8°$ for the remaining three (183–380 GHz). Antenna patterns have been simulated considering the antennas' specifications, resulting in first sidelobes lower than -27-dB level and main beam efficiencies within 98.9 ± 0.2 (slightly depending upon the channel). The remaining radiometer operates as an infrared broadband channel at $10.6\,\mu m$.

B. External Targets

The two external targets (Fig. 1) are identical and were specially designed for the GSR [26]. Each target has an aperture of approximately 67×43 cm and consists of a roof-shaped aluminum frame internally lined with absorbing foam. The foam is shaped in pyramids with two different scales of roughness to provide less than 0.1% reflection in the 18–500-GHz range, which covers the entire set of GSR frequencies. Heating (and, respectively, cooling) elements are placed behind the foam of the hot (cold) target, together with fans operating to

TABLE I
NOMINAL CENTRAL FREQUENCY FOR GSR CHANNELS

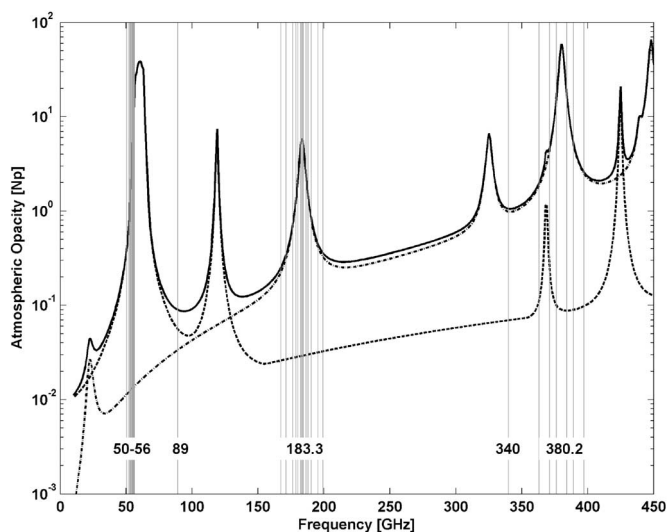|	50-56 GHz	89 GHz	183 GHz	340 GHz	380 GHz	10.6 μm
Chn 01	50.3	89 V	183.3±0.55	340 V	380.197±4	10.6±6
Chn 02	51.76	89 H	183.3±1	340 H	380.197±9	
Chn 03	52.625		183.3±3.05		380.197±17	
Chn 04	53.29		183.3±4.7			
Chn 05	53.845		183.3±7			
Chn 06	54.4		183.3±12			
Chn 07	54.95		183.3±16			
Chn 08	55.52					
Chn 09	56.025					
Chn 10	56.215					
Chn 11	56.325					

Fig. 3. Atmospheric opacity computed for a standard Arctic winter atmosphere (IWV = 0.45 cm), using the absorption model in the study in [27]. The dash-dotted line represents the opacity due to atmospheric water vapor. The dotted line represents the opacity due to oxygen, while the solid black line is the total opacity. The vertical lines indicate the spectral location of GSR channels.

the 50–56-GHz channels are located in the strong oxygen-absorption band and allow for atmospheric-temperature estimates [31]. The 183- and 380-GHz channels are located on the sides of two strong water-vapor absorption lines (corresponding to different opacity depending upon distance from the line center) and allow for accurate observations of low water-vapor contents typical of the Arctic [23]. The horizontal (H) and vertical (V) polarization channels at 89 and 340 GHz are located in fairly transparent atmospheric regions (windows) and thus allow the study of cloud properties through the measurement of the emission and depolarization ratio. The radiometric sensitivity at 1-s integration time (as defined in the study in [30]) for GSR microwave channels was measured in the laboratory at room temperature (∼25 °C) before the experiment and is listed in Table II.

III. EXPERIMENTAL SETUP

The first deployment of the GSR occurred during the Arctic Winter Radiometric Experiment 2004 [34], held from March 9 to April 9 at the Department of Energy Atmospheric Radiation Measurement (ARM) Program's North Slope of Alaska (NSA) site in Barrow, AK (71° N, 156° W).

A. Arctic Winter Radiometric Experiment 2004

The Arctic Winter Radiometric Experiment was carried out by the Microwave System Development Division of NOAA/PSD, in collaboration with ARM, the Argonne National Laboratory, and Montana State University. The experiment was based on the deployment of the principal instrument, the GSR, at the operational ARM NSA site. At this site, ARM operates a variety of remote and *in situ* sensors, which includes, but is not limited to, a dual-channel microwave radiometer (MWR), a 12-channel MWR profiler (MWRP), and a radiosonde-launching facility. Further information about the ARM NSA site with a detailed description of the operational instrumentation is available online at http://www.arm.gov/. The GSR was installed on March 9, 2004, and collected continuous observations until April 9, 2004, yielding about a month of data.

B. Mode of Operation

The GSR was mounted on the northeast corner of the skydeck, which is the platform supporting the operational ARM NSA instruments [Fig. 1(b)]. With this experimental

maintain a steady air flow within the enclosure and so reduce thermal gradients. The temperature of each target is continuously measured by 16 thermistors distributed along the volume, and a closed-loop controller is used to keep the target nominally within 0.1 K with respect to the set temperature. The target, heaters, fans, and thermistors are enclosed in a polystyrene box, insulating the system from the surrounding environment [24]. The microwave-emission temperature of the targets is, thus, precisely calculable using measurements of the physical temperature of the foam. When mounted on the GSR housing, the absorbing side of each target faces toward the scanhead, as in Fig. 1. During operation, the two boxes are kept at different temperatures, providing the two reference points needed for complete calibration.

C. GSR Channels

The complete set of GSR microwave channels, listed in Table I, was selected for the simultaneous retrieval of atmospheric-temperature profile, water-vapor content, cloud liquid path, and cloud-depolarization ratio. In particular, referring to the spectrum of the atmospheric opacity (τ) in Fig. 3,

TABLE II
SENSITIVITY (IN KELVIN) AT 1-S INTEGRATION TIME FOR GSR MICROWAVE CHANNELS

	55-56 GHz	89 GHz	183 GHz	340 GHz	380 GHz
Chn 01	0.096	0.037	0.212	0.141	0.131
Chn 02	0.065	0.037	0.170	0.141	0.106
Chn 03	0.076		0.127		0.184
Chn 04	0.069		0.099		
Chn 05	0.095		0.085		
Chn 06	0.089		0.071		
Chn 07	0.076		0.057		
Chn 08	0.098				
Chn 09	0.083				
Chn 10	0.184				
Chn 11	0.170				

setup, the GSR scanhead had a completely unobstructed view along the west–east direction. The GSR has a flexible and software-programmable angular scanning sequence. During the experiment, the following cycle was repeated every 2 min. The sequence starts with the scanhead inside the calibration house, viewing the calibration targets. Then, the trolley slides out of the housing and moves to the atmospheric scanning position. In this position, the scanhead rotates from 15° to 165° elevation angle, stopping at selected angles (dwells) corresponding to 3, 2.5, 2.0, 1.5, and 1.0 air masses (the air mass at any elevation angle is defined as the atmospheric opacity at that angle normalized by the atmospheric opacity at zenith). Between the dwells, the scanhead moves to the next scan position while continuously collecting data. Thus, during one complete cycle, the radiometers acquire both continuous and dwell observations of the atmosphere plus two-point calibration data. The basic A/D sample time is 0.6 ms, and data are averaged to get a recorded sample each 14 ms.

IV. CALIBRATION

A. Background

Calibration is a key issue for MWRs, because the quantity that is intended to be measured—the natural emission of a given body—is usually smaller than the thermal noise produced by the instrument itself. A standard calibration method consists of moving the antenna to observe alternately two external reference loads, whose emission is known to high accuracy, and determining the calibration coefficients (gain and offset) based on the difference of the instrument output. Unfortunately, the antenna movements are much slower than the time scale with which high-frequency gain fluctuations occur, and thus, such a method cannot account for them.

Another conventional method [9], [13] is based on a switch placed between the antenna and the receiver which quickly alternates the receiver input between the external scene and two internal reference loads. This method accounts for internal-gain fluctuations, but part of the instrument (such as the antenna, lens, and waveguides) necessarily remains out of the calibration loop; therefore, temperature variations in these components are not monitored.

Another way to obtain calibration is the so-called "tipping-curve" method [14], which consists of sky observations at different elevation angles, that relies on the assumption of a plane-parallel horizontal stratified atmosphere. It has been demonstrated that this method provides high absolute accuracy [3], [23], although it presents some limitations. In practice, it can be applied only to channels with low opacity during clear-sky conditions. Moreover, the tipping-curve method may provide just one of the two coefficients needed for complete calibration. Therefore, this method is used only as a correction applied to one of the two coefficients obtained from some other method.

B. GSR Calibrations

As discussed, none of the above-listed methods alone is able to establish accurately the complete end-to-end calibration of a MWR. For this reason, MWRs are usually calibrated using a combination of the described methods. In particular, the GSR design allows all three methods introduced above, as discussed in the following sections.

1) Internal Calibration: Each GSR is equipped with an independent switch, located between the lens and the receiver. During normal operation, the input of each receiver is alternately switched between the external scene and two internal references. In the case of 55- and 89-GHz radiometers, we use a triport ferrite circulator as a switch, a termination (noise attenuator) as cold reference, and a noise diode as hot reference (shown in Fig. 4 for 55 GHz). However, for frequencies above 150 GHz, no suitable electric switch exists. Thus, for 183-, 340-, and 380-GHz radiometers, an electromechanical system using a rotating mirror in front of the horn antenna and two blackbody targets was developed at NOAA/PSD (as shown in Fig. 5 for 183 GHz).

A time series of a few internal cycles for the 51.76-GHz channel is depicted in Fig. 6. The top panel shows the ferrite-switch state, which alternates between scene (0) and calibration (1) position about every 140 ms. As illustrated in Fig. 4, a two-port switch, a p-i-n diode, is located between the noise generator and the attenuator. When the p-i-n diode is OFF, the switch is open, and the available power corresponds to the thermal noise emitted by the attenuator (indicated as the cold load). Conversely, when the p-i-n diode is ON, the switch is closed, and the available power is a combination of the physical temperature of the attenuator and the power emitted by the noise generator (hot load). The combination of the ferrite-switch state (top panel) and the p-i-n-diode state (second panel) generates the calibration state, or Cal state (third panel), which can assume the following three values: one (hot load), two
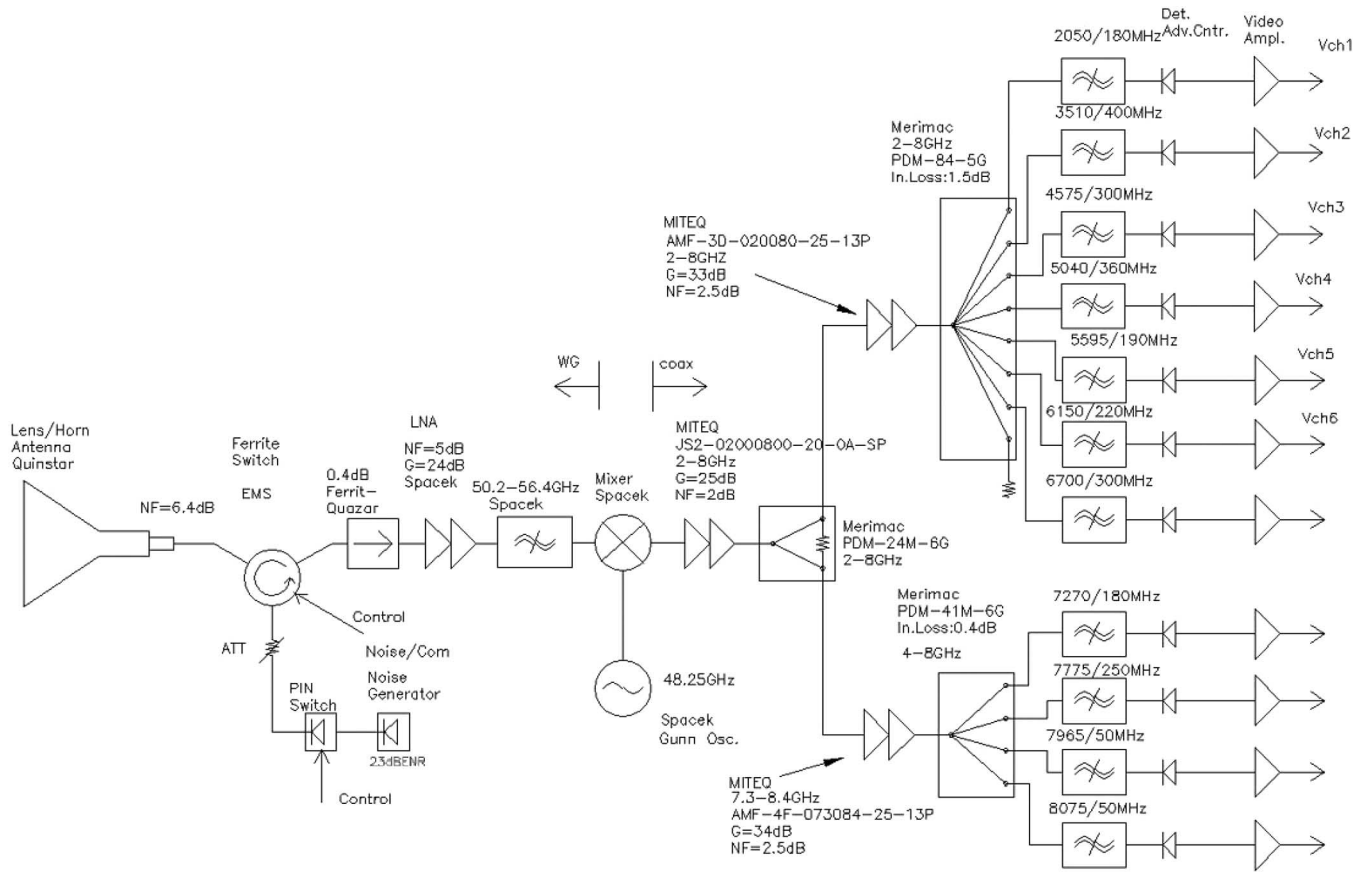
Fig. 4. Block diagram of 55-GHz GSR . The same diagram applies for the 89-GHz radiometer except that an orthomode transducer is located between the antenna and the internal calibration switch to separate the horizontal and vertical polarizations.
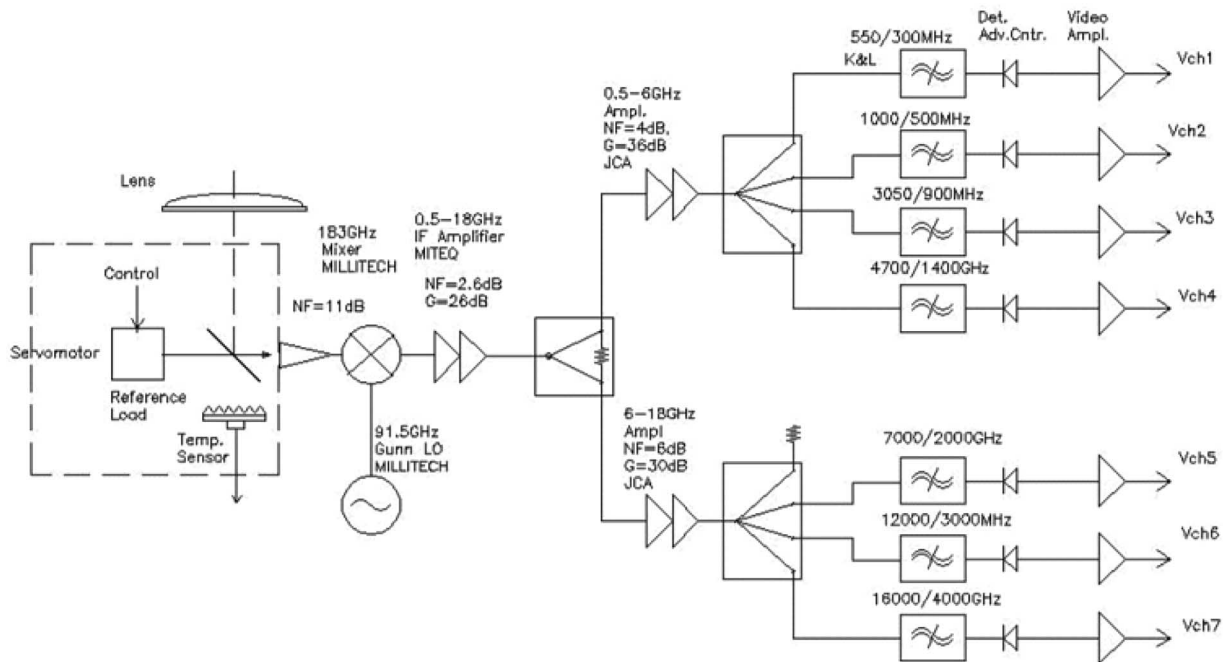

Fig. 5. Block diagram of 183-GHz GSR. A similar diagram applies for the 380- and 340-GHz radiometers, except that, for the latter, an orthomode transducer is located between the antenna and the internal calibration switch to separate the horizontal and vertical polarizations.

(cold load), and seven (scene observation). The effect of the internal calibration switching on the output signal is shown in the bottom panel. Only periods indicated by S (scene) are used for atmospheric study, while periods indicated by H (hot) and C (cold) are only used for the calibration. A two-point calibration is available every 420 ms, while a complete cycle takes
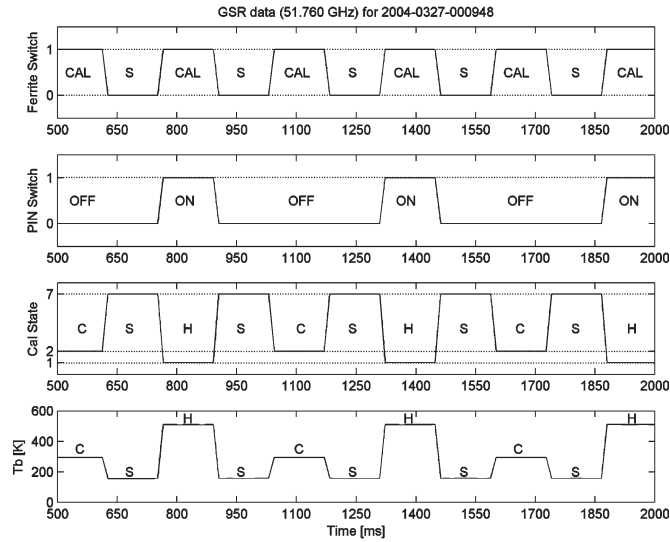
Fig. 6. Time series of internal calibration cycles. Only the 51.76-GHz channel is shown here.

about 560 ms. The same internal calibration cycle is used for the 89-GHz radiometer.

For 183-, 340-, and 380-GHz radiometers, rotating mirrors are used instead of electric switches [10]. In order to obtain a short switching time, we used a vibration-free servomotor with a high angular acceleration and velocity (2410 rad/s). An alignment tool was designed and fabricated at NOAA/PSD to precisely locate the position of the mirror along the motor shaft. Two high-emissivity pyramidal iron-epoxy blackbodies are used as references for each radiometer. The hot calibration target includes the blackbody, a thermal conductor in the form of an aluminum plate, two thermistors to monitor the target temperature, a heating element, and insulating foam. The cold calibration target includes the blackbody, a thermoelectric cooler, two thermistors, and the insulating foam. The complete cycle takes about 1288 ms.

For each of the GSR channels, the brightness temperature (T_b) of the scene view is estimated via the standard hot–cold method [30] by using the voltages measured during the internal calibration. The periods for typical internal calibration cycles and the percentage of time spent for each position are listed in Table III, while a summary of the used equations is given in Appendix I-A.

2) External Calibration: The internal calibration discussed in the previous section does not include any contribution by the components that are located before the input switch, such as the lens and waveguides. The contribution of these components can be measured in the laboratory but might vary during the deployment for a variety of reasons, including temperature fluctuations and small particles over the lens. Thus, such contributions need to be monitored and taken into account during the overall calibration; this can be done by pointing the radiometers toward external references that include all the components in the calibration process. Therefore, the GSR system includes two external reference targets [Fig. 1(a)]. During normal operation, the GSR scanhead points alternately toward the sky, and the two targets, providing a complete end-to-end calibration every cycle, are set to 2 min during the experiment. The thermal

stability of the external targets is typically within 0.1 K over 2-min periods due to the large heat capacity of the aluminum frames behind the absorber and thick layer of foam insulation. The thermodynamic temperature of the antennas is measured and stored, and during the experiment, 2-min fluctuations were found to be smaller than 0.1 K. The time intervals, with percentage value, spent on various positions per each scan cycle are given in Table IV, while the used equations are given in Appendix I-B.

3) Tipping-Curve Calibration: The tipping-curve method relies on a linear relationship between atmospheric opacity (τ) and air mass (a) under the assumptions of low absorption and a horizontally stratified atmosphere. By relating τ, which is estimated by measurements of T_b, to a at two or more elevation angles, the tipping-curve method can provide a correction to a single calibration parameter, as carefully discussed in the study in [14]. This last step might seem somewhat redundant, since the complete end-to-end calibration is provided by internal and external calibrations. Conversely, it is extremely useful in correcting for other effects that might have been neglected, such as detector nonlinearity or uncertainties in the external target radiative temperature. In general, the tipping-curve method is used as a compound correction that adjusts for departures of the system from the ideal model. However, this method presents two major limitations: first, it can be used only under the assumption of homogeneous and horizontally stratified atmosphere, meaning clear sky with no significant horizontal gradient; second, mapping T_b into τ involves an error that in first approximation increases as T_b approaches the mean radiative temperature T_{mr} [30]. Therefore, the tipping-curve method is applicable only to those channels that exhibit a relatively low T_b. Fortunately, these are the channels that need it the most, because their T_b fall much below the range covered by the calibration references (see Section IV-D). Nevertheless, even for relatively opaque channels, we can select a subset of angles at which T_b is low enough to guarantee a maximum tolerable error in τ and apply the tipping-curve method to this subset.

During the sky observations, the GSR antennas scan the atmosphere from 15° to 165° in elevation, thus allowing the tipping-curve correction every cycle (2 min). The quality of the tip curves is checked, discarding cases in which either the correlation coefficient of the linear fit [20] or the standard deviation of the equivalent zenith T_b [3] fails the comparison with a threshold (whose value depends upon the channel). The set of tipping curves that passed the quality checks was used to compute the correction factor. In the case of channels with relatively low attenuation (50.3, 51.76, 89, 183 ± 7/12/16, and 340 GHz), we apply the correction instantaneously, i.e., every time a good tip is available. At some other channels (52.625–53.845, 183 ± 0.5/1.0/3.0/4.7, and 382.2 ± 4/9/17 GHz) for which a subset of eligible angles was found only occasionally, we determined a statistical value for the correction coefficient and we use it throughout the experiment. For the remaining channels (54.4–56.325 GHz) for which the measured T_b approaches T_{mr}, no scan was found eligible for tipping curve; however, at these channels, T_b is close to the cold reference, and we can accurately rely on the external

TABLE III
TYPE OF INPUT SWITCH AND TYPICAL PERIODS OF TIME (PERCENTAGE) SPENT ON THE SCENE
AND INTERNAL LOADS OBSERVATION FOR ONE INTERNAL CALIBRATION CYCLE

	50-56 GHz	89 GHz	183 GHz	340 GHz	380 GHz
Input internal switch	Ferrite circulator	Ferrite circulator	Rotating mirror	Rotating mirror	Rotating mirror
1 cycle (msec)	560	560	1288	1288	1288
Scene (%)	50.0	50.0	45.8	46.7	45.4
Hot Target (%)	25.0	25.0	22.9	23.4	22.7
Cold Target (%)	25.0	25.0	22.9	23.4	22.7
Transit (%)	0.0	0.0	8.4	6.5	9.2

TABLE IV
TIME INTERVAL, AND PERCENTAGE VALUE, SPENT IN VARIOUS POSITIONS PER EACH 2-min SCAN CYCLE. CONSIDERING THE
SWITCHING FOR THE INTERNAL CALIBRATION, THE DUTY CYCLE REDUCES BY 1/2 FROM THAT GIVEN IN THIS TABLE

	External hot target	External cold target	Total dwell positions	Movement during sky scanning	Movement inside housing
Time (sec)	4	4	22	79	10
Time (%)	3.4	3.4	18.5	66.4	8.4

TABLE V
TYPICAL TEMPERATURES OF THE INTERNAL REFERENCES DURING THE EXPERIMENT

	50-56 GHz	89 GHz	183 GHz	340 GHz	380 GHz
Tcold (K)	295	297	242	246	250
Thot (K)	507	349	348	346	335

calibration. The equations and other details of the tipping-curve method are given in Appendix I-C.

C. Settings

During the deployment of the GSR at the Arctic Winter Radiometric Experiment, the following settings were adopted. The temperature of the internal references was controlled to guarantee a large difference between hot and cold loads; typical values are reported in Table V. The temperature of the external cold target was left floating with ambient temperature (from $-40\ °C$ to $-20\ °C$), while the external hot target temperature was set to 70 $°C$, covering about a 100 $°C$ dynamic range. A typical time series of GSR observations is shown in Fig. 7 for the 51.76-GHz channel; raw voltages have been calibrated following the steps discussed in Section IV-B, while the measurements taken during internal reference observations are not shown. The top panel shows T_b measured during a period covering approximately two complete scans, while in the bottom panel, we find the hardware-trigger (HT) signal, which assumes a different integer value for each scanhead position. Referring to Fig. 7, the following is a complete cycle.

1) A new scan begins with the scanhead inside the housing, observing the external hot target for 1 s (H). The corresponding HT value is one, as shown in the bottom panel. The observed T_b is about 343 K, which corresponds roughly to the physical temperature of the target (70 $°C$).
2) The scanhead moves toward the next position. The HT value is three, which means the scanhead is rotating while inside the housing.
3) The scanhead observes the external cold target for 4 s (C), indicated with a two by the HT. The observed T_b is about 250 K ($-23\ °C$).

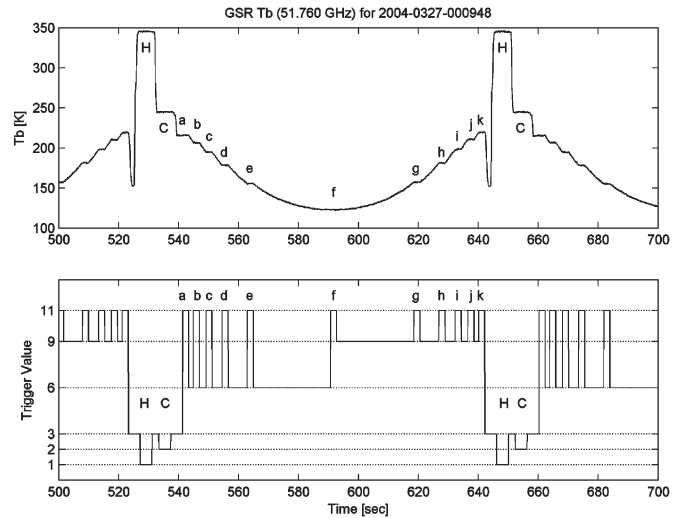Fig. 7. (Top) Times series of GSR observations at 51.76 GHz. (Bottom) HT value indicating angular position.

4) The scanhead moves to the next position (HT = 3), while the trolley moves out of the housing.
5) The trolley reaches the sky-scan position. The scanhead starts to scan the west side (indicated by HT = 6), stopping at selected dwell positions (HT = 11) for 2 s. The dwell positions indicated by a, b, c, d, and e corresponding to 3.5, 3.0, 2.5, 2.0, and 1.5 air masses, respectively. The observed T_b's are fairly constant during each 2-s dwell position, while they decrease with decreasing air masses. Note that while moving from one dwell position to the next, the scanhead collects continuous observations.

6) The scanhead reaches the zenith position, indicated by f, and dwells for 2 s. Zenith position corresponds to one air mass, and the observed T_b shows a minimum.

7) The scanhead starts the east scan (HT = 9), stopping at five selected dwell positions (HT = 11), corresponding to 1.5, 2.0, 2.5, 3.0, and 3.5 air masses ($g, h, i, j,$ and k). The observed T_b increases with the increasing air mass.

8) The scanhead moves toward the next position, while the trolley slides back into the housing (HT = 3). The observed T_b shows a sharp decrease due to the scanhead rotation outside the housing and, then, a rapid increase when the scanhead is finally back to initial position (HT = 1), corresponding to hot target observation (H).

During the Arctic Winter Radiometric Experiment, the period required to complete the entire cycle was set to 2 min.

D. Expected Accuracy

The implementation of the three steps of calibration in cascade is expected to provide high accuracy during both clear and cloudy conditions. The internal calibration is basically used to monitor high-frequency gain fluctuations and to compensate for the effect of convective flows within the scanhead that may modulate the calibration during the scan. The stability of internal loads depends on their physical temperature, which does not change significantly during the internal calibration cycle ($\sim$1 s). Allan variance [1] analysis of the radiometers' output showed expected decreasing variance out to averaging intervals of at least 10 s, indicating that the instrument parameters were stable within the calibration cycle [25]. However, internal calibration is not required to provide high absolute accuracy, since its output is then fully calibrated with external and tipping-curve methods. Therefore, estimating the absolute accuracy of GSR measurements means an analysis of the error sources involved with the combination of external and tipping-curve calibration.

Several factors introduce errors in a two-point external calibration, as carefully discussed in the study in [22]. In the case of GSR, these reduce to uncertainties in target temperatures, detector nonlinearity, and radiometer noise. Regarding the target temperatures, the 12 thermistors distributed within the volume of the foam usually agreed within 0.1-K rms for the cold target and 0.3-K rms for the hot target. These would cause an error in T_b smaller than 0.3 K in the range covered by the hot and cold references, but for lower T_b, the error would increase from 0.1 to 0.8 K as it gets farther from the cold reference. The detector nonlinearity was checked in the laboratory using a two-attenuator method in a power range from -35 to -15 dBm and found to be within 1%. This uncertainty would cause negligible error within the calibration range, but for lower T_b's, the error increases to as much as 0.6 K. This number represents a worst case value, as it is slightly dependent upon the channel through the system noise temperature. The radiometer noise contributes to the calibration error with random components on different time scales. The radiometric sensitivities in Table II were measured in the laboratory with the radiometers observing a stable target at room temperature ($\sim$25 °C), and do not account for additional noise due to internal switching, scanning, and environmental conditions during deployment. The budget for

random errors due to gain, voltage, and target-temperature fluctuations experienced during the experiment is given in Table VI. For most GSR channels, the random component is within 0.4–1.2 K, which is comparable to the ones in the study in [22]. Nonetheless, there are a few undesired exceptions. In particular, 183 ± 0.5, 183 ± 1, and 183 ± 7 channels show larger noise than expected, subsequently identified as due to radio-frequency interference. Furthermore, the 340-GHz radiometer was affected by excessive noise, probably related to hardware problems in the front end. Currently, some aspects of the GSR are being redesigned to eliminate these problems.

In summary, besides random errors, the external calibration is quite accurate for T_b close to the calibration range, although it involves errors of the order of 1 K for lower T_b's due to target temperature uncertainties and detector nonlinearity. However, by applying tipping-curve correction to rather transparent channels (corresponding to low T_b), we virtually add a calibration point at 2.7 K (the cosmic radiation), limiting the uncertainty to a few tenths of a degree. The error sources involved in the tipping-curve method are carefully discussed in the study in [14] and are here adapted to the GSR (see Appendix I-C). The air-mass–angle relationship (32) assumes plane-parallel atmosphere and involves an error due to the curvature of the Earth. This effect can be largely accounted for by introducing a correction based on an effective height H, which has been determined for each GSR frequency. After applying this correction, the residual error due to the Earth's curvature should be less than 0.1 K. The effect of finite antenna beamwidth is accounted for assuming a Gaussian beam and using the correction suggested in the study in [14] to the T_b calibrated with external references, before the tipping curve is applied. Considering this correction, the calibration error arising from finite antenna beamwidth should be on the order of 0.1 K. Errors associated with uncertainties in pointing angle can be substantially reduced by using tipping-curve data taken on both sides, as we do with GSR scans. Since the pointing angle is known within $\pm 0.5°$, we estimate this uncertainty to be on the order of 0.1 K. The effect of uncertainty in the radiometric equation offset [in our case, the spill-over radiance $B_{\nu,A}$ in (29)] can be estimated by performing a tipping curve on the original data and on the data that have been shifted artificially by adding an increment to the offset. It was found that the tipping curve effectively compensates for the shift, such that the resulting error is much smaller than the artificial increment. As long as the temperature corresponding to $B_{\nu,A}$ is known within ± 5 K, this effect remains within 0.1–0.3 K, slightly dependent upon the channel. Random noise also affects the accuracy of the tipping-curve method. Considering the numbers in Table VI and about 71 samples per 2-s dwell interval (14-ms samples with a duty cycle of 0.5), and propagating the resulting noise into the tipping-curve-calibration equation, the contribution remains within 0.1 K (0.2 K for 340-GHz channels). The concept of mean radiating temperature [see (30)] is used in the tipping-curve calibration to map T_b into opacity τ. For low brightness temperatures, uncertainties in T_{mr} result in small uncertainties in τ. As T_b becomes larger, uncertainties in T_{mr} significantly affect the estimate of τ and, thus, the accuracy of tipping-curve calibration. Han and Westwater [14] showed that uncertainties

TABLE VI
RANDOM NOISE (IN KELVIN) FOR GSR MICROWAVE CHANNELS DURING THE ARCTIC WINTER RADIOMETRIC EXPERIMENT 2004

	50-56 GHz	89 GHz	183 GHz	340 GHz	380 GHz
Chn 01	0.475	0.555	2.863	2.422	1.302
Chn 02	0.532	0.558	1.600	2.468	1.163
Chn 03	0.501		1.080		1.209
Chn 04	0.298		0.792		
Chn 05	0.385		1.451		
Chn 06	0.485		0.453		
Chn 07	0.378		0.449		
Chn 08	0.443				
Chn 09	0.424				
Chn 10	0.610				
Chn 11	0.662				

in T_{mr} can be reduced by a factor of two by predicting it from simultaneous measurements of surface air temperature (T_s). However, they admit that T_{mr} prediction from T_s is often poor when large temperature inversions occur. During the experiment, temperature inversions as large as 10 K in the lowest 2 km were observed by radiosondes and MWRP. Using T_s from the surface sensor on the MWRP and T_{mr} at GSR channels simulated from radiosonde data, we found an accuracy of T_{mr} prediction from T_s within 2–4 K rms, depending upon the frequency and considered air mass. As a further step, Han and Westwater [14] suggest that the T_{mr} estimate can be improved by considering boundary-layer temperature profiles observed by a remote-sensing instrument, such as an MWR operating in the 50–60-GHz band. More directly, T_{mr} can be predicted through linear regression based on T_b observations. Considering that the GSR has 11 channels (50.3–56.325 GHz) in that band, we could use T_b calibrated with the external targets to estimate T_{mr}. Unfortunately, the 50–56-GHz GSR experienced hardware problems during the experiment that made a considerable part of the data unavailable. On the other hand, the MWRP operated for the entire period only a few meters from the GSR. Thus, we selected T_b at four MWRP channels (54.94, 56.66, 57.29, and 58.80 GHz) in the oxygen band plus the surface air temperature as predictors. The most opaque channels were chosen in order to keep the estimate valid during both clear- and cloudy-sky conditions. Furthermore, we performed an empirical orthogonal function (EOF) analysis of the set of predictors to optimize the training despite the relatively small sample size (109). Of the original five predictors, only three EOF were found to be significant over the considered level of MWRP random noise (0.3 K). As expected, uncertainties in the T_{mr} estimate are significantly reduced with respect to prediction based on T_s only. By using the described approach, the accuracy of the T_{mr} estimate for the set of GSR channels is within 0.5–1.5 K, depending upon the frequency and considered air mass. Equivalent results are expected when using GSR channels as predictors. This accuracy should limit the calibration error associated with T_{mr} uncertainties to a contribution on the order of 0.1 K.

Finally, the total uncertainty for a single observation would result from the combination in quadrature of all the systematic and random components. For most of the GSR channels, the resulting total uncertainty is within 1 K and for all but three channels is within 1.5 K. Random error is the dominant component for the three channels showing the highest uncertainty (2.5–3.0 K). These large errors were due to radio-frequency interference for the 183 ± 0.5-GHz channel and to problems with the design of the front end for 340-GHz (H and V) channels. These problems are expected to be eliminated with the current upgrade of the scanhead, eventually keeping the total uncertainty for all channels within 1.5 K.

V. RESULTS: SELECTED EXAMPLES

During the Arctic Winter Radiometric Experiment, observations were collected for about one month. The GSR and the ARM NSA operational instrumentation (MWR and MWRP) worked almost continuously with a small percentage of downtime. The atmospheric conditions varied over a fairly large range of surface temperature, water vapor, and cloud LWP. The expectations of encountering very dry and cold conditions, possibly with extreme periods of IWV and T_s lower than 0.1 cm and $-30\,°C$, respectively, were satisfied.

A. Angular and Spectral Signature

During normal operation, the GSR continuously performs cycles, as in Fig. 7, acquiring measurements at 26 channels. As shown in Fig. 3, across the GSR channels, the atmospheric opacity differs by about two orders of magnitude. For this reason, we expect to see T_b as low as 15 K for transparent channels (e.g., 89 GHz), while as high as saturation ($\sim$250 K) for very opaque channels (e.g., 56.6, 183 ± 0.5, and 380 ± 4 GHz).

As an example, Fig. 8 illustrates a time series of three consecutive atmospheric scans as observed by the GSR channels. For clarity, we plot the measurements from each individual radiometer in a different panel: 1) 55; 2) 89; 3) 183; 4) 340; and 5) 380 GHz. In Fig. 8, we can see both the spectral and the angular signature of the different GSR channels. Let us consider, for example, the 50–56-GHz channels [Fig. 8(a)]. For each atmospheric scan, T_b's at the 11 channels are symmetric with respect to the half-scan position, which corresponds to zenith. This is consistent with the assumption of a homogeneous atmosphere; in such a case, the atmosphere is symmetric with respect to the azimuth angle, and thus, the west scan is equivalent to the east scan.

Concerning the spectral signature, Fig. 3 shows that, in the 50–56-GHz band, we move from relatively low absorption to very high absorption as we approach the center of the 60-GHz absorption band. For frequencies located away from the center,
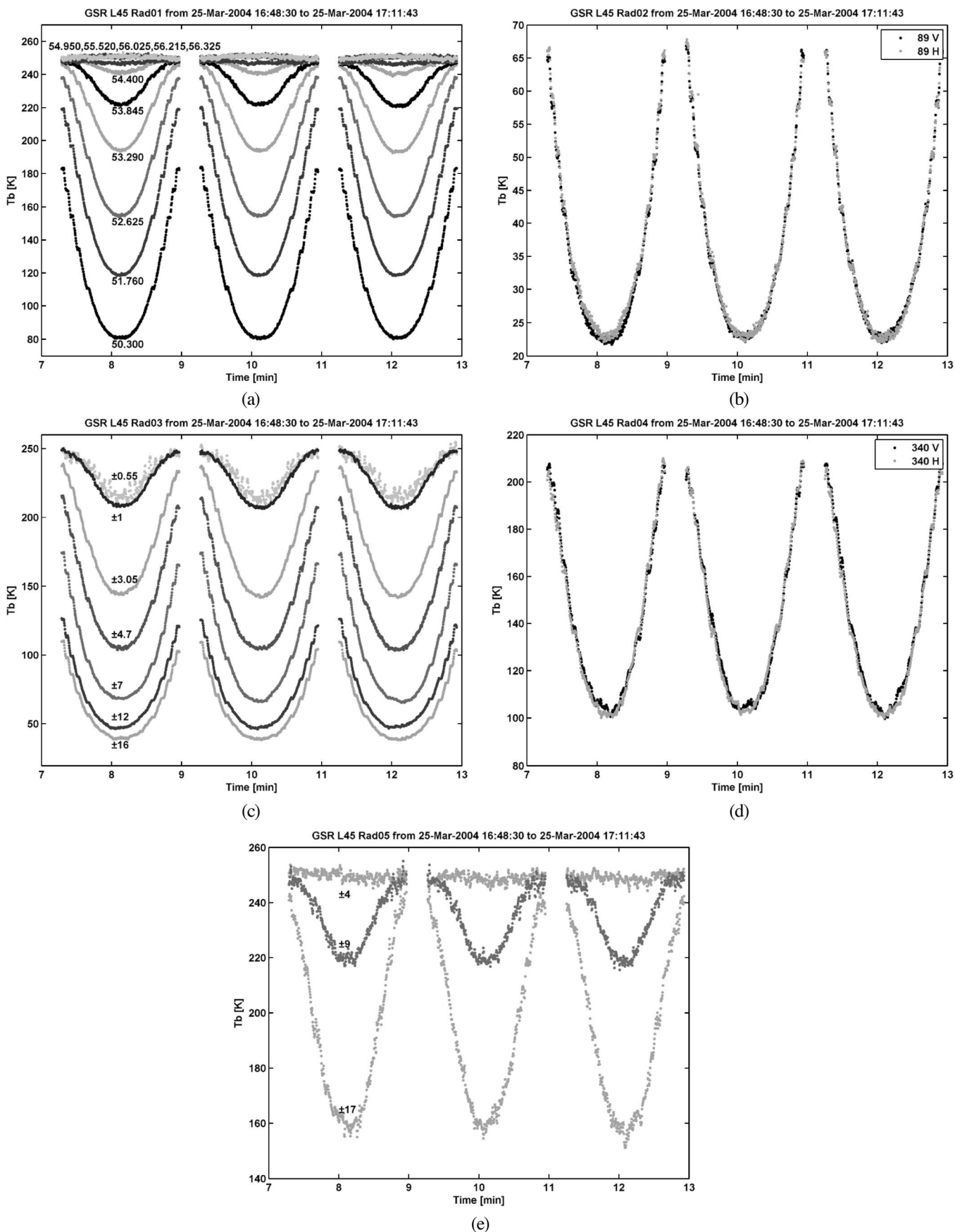
Fig. 8.   Angular and spectral signature of GSR observations. (Top) The 55- and 89-GHz channels. (Middle) The 183- and 340-GHz channels. (Bottom) The 380-GHz channels. (Both sides) For each cycle, the antennas scan from 15° to 165° elevation angle, stopping at selected dwell positions corresponding to 3, 2.5, 2.0, 1.5, and 1.0 air masses.

the corresponding channels are rather transparent. In this case, as the elevation angle increases from 15° to 90° (zenith), the observed T_b comes from atmospheric levels at increasingly high altitude. If we consider that in the first approximation, then the temperature of the atmosphere decreases with height at 6.5 K/km, the T_b measured by a transparent channel has its minimum at zenith. This explains the behavior of transparent channels (e.g., 50.3 GHz) in Fig. 8(a). As the frequency gets closer to the center of the 60-GHz absorption band, the channels become increasingly more opaque, showing less variation with the elevation angle. For high-frequency channels (55 GHz and higher), the opacity is so high that the observed T_b comes entirely from the first levels (height is < 1 km). Particularly in the Arctic, these levels often present a temperature inversion. In the presence of a temperature inversion, the opaque channels would show the opposite angular trend (i.e., maximum T_b at zenith) compared to the transparent channels; because of the relatively short path, they can penetrate into the atmosphere. This explains the behavior of 55–56-GHz channels in Fig. 8(a).

Similar considerations apply for the other GSRs shown in Fig. 8(b)–(e). In particular, channels corresponding in Fig. 3 to low absorption (e.g., 89, 183 ± 16, 340, and 380 ± 17 GHz) show a large dynamic range during the atmospheric scan, with a T_b minimum at zenith. For channels with moderate absorption (e.g., 183 ± 3 and 183 ± 4.7 GHz), there is a substantial decrease in the dynamic range, although the minimum T_b is still at zenith. For very opaque channels (e.g., 380 ± 4 GHz), the absorption is so strong that almost no angular variation is observed.

Note that the 183.3- and 380.2-GHz water-vapor-absorption lines are so strong that they would be saturated, i.e., unusable, in moister environments, for example, other ARM sites at middle or tropical latitudes. However, in extremely dry environments, such as the polar or mountain regions, these frequencies are usually not saturated and offer their greatly enhanced sensitivity. This is indeed the reason why submillimeter-wave radiometry is well suited for deployment in very dry environments, such as the polar and high-altitude regions.

B. Comparison With Radiosonde Observations

In order to validate the GSR observations, we show a comparison with independent measurements from balloon-borne radiosonde observations (RAOBs). During the experiment, four RAOBs per day were launched from the facility hosting the personnel and one per day from the site hosting the instrumentation. A standard way to compare RAOBs and radiometric measurements is to process the atmospheric temperature, humidity, and pressure profiles with a radiative-transfer model (RTM) in order to compute the simulated T_b illuminating the antennas. The simulated T_b's depend on the assumptions underlying the RTM, which in clear-sky conditions, mainly involves the parameterization of the spectroscopy used to resolve the gas-absorption coefficient. Several microwave absorption models are available in the literature, including the ones described in the study in [18], [19], [21], and [27], and a concise analysis of their different parameterizations is given in [15]. The study of gas absorption models through comparison with well-

calibrated data is indeed one of the major goals of the Arctic Winter Radiometric Experiment. The scope of this paper is to describe the technique for obtaining well-calibrated data, while a thorough comparison with different absorption models is currently ongoing. Nevertheless, to give a sense of the uncertainty associated with model parameterization and, at the same time, to keep our validation unbiased, we compare GSR data with RAOBs processed with all the absorption models aforementioned. This comparison is shown in Fig. 9 for 24-h time series of zenith views. Again, we divided the observations from the five radiometers into five different panels [Fig. 9(a)–(e), same order as in Fig. 8]. The GSR measurements are shown in dots, while the simulated T_b's, computed from RAOBs at GSR frequencies, are interpolated with a solid line just to highlight the diurnal trend. Although this is just a qualitative comparison, we note significant differences between the models, leading to different agreement with the GSR observations. These are in fact the basis for an analysis of atmospheric absorption models. In general, we see that GSR data usually fall within the range covered by RAOBs simulations, with the exception of four channels in the oxygen band and both channels (H and V) at 89 GHz. In fact, the four high-frequency channels of the 55-GHz radiometer (55.520–56.325) show a consistent 2.5-K positive bias with respect to simulations (which agree within 0.1 K regardless of the absorption model). This issue was subsequently identified as a hardware problem; in fact, these four channels are physically separated from the other seven (Fig. 4) and subject to poorer temperature stabilization that exposed them to temperature variations during scanhead rotation. Upgrades currently being made on the GSR hardware should eliminate this problem for future deployments. For 89-GHz H/V channels, the situation is not as clear. Depending upon the absorption model, measurements show a 2–4 K positive bias with respect to simulations, although the two polarizations agree well with each other. At the present time, we are not able to identify this bias as related to hardware problems. Note that the bias remains consistent throughout the experiment, and thus, it cannot be caused by direct solar radiation; moreover, the sun usually appeared low over the horizon in the south direction, while the antennas were scanning along the west–east direction. In addition, the contribution caused by galactic emission is low (∼mK) at these frequencies. However, there are indications in the open literature that oxygen coupling coefficients are not accurately known at low temperatures [2], which may cause atmospheric absorption at this frequency to be underestimated in cold environments [15]. Nonetheless, the GSR is currently undergoing further characterization to check for unexpected hardware characteristics. For example, in the case of unexpected large antenna backlobes, emission from the ground would contaminate the sky radiance, affecting, particularly, transparent channels such as 89 GHz.

C. Comparison With Ancillary Data

An interesting feature of the GSR is definitely the continuous in-angle scan of the atmosphere. This feature gives the possibility of comparing measurements with observations at different elevation angles, opening a new prospect for the study
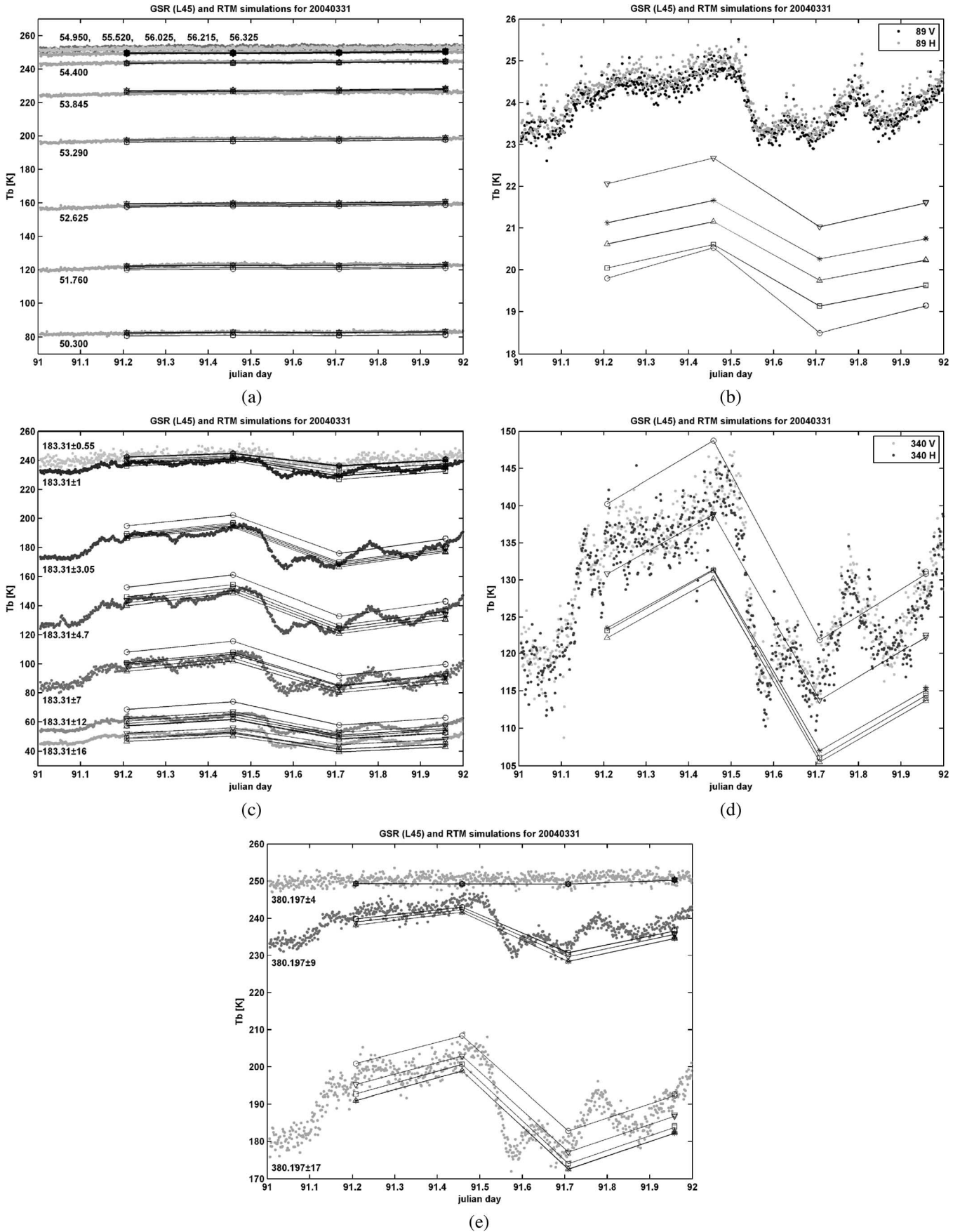
Fig. 9. Comparison of simulated and measured zenith T_b. Simulations are based on absorption models in (squares) [18], (circles) [19], (upward triangles) [27], (stars) [28], (downward triangles) [21]. (Top) The 55- and 89-GHz channels. (Middle) The 183- and 340-GHz channels. (Bottom) The 380-GHz channel.
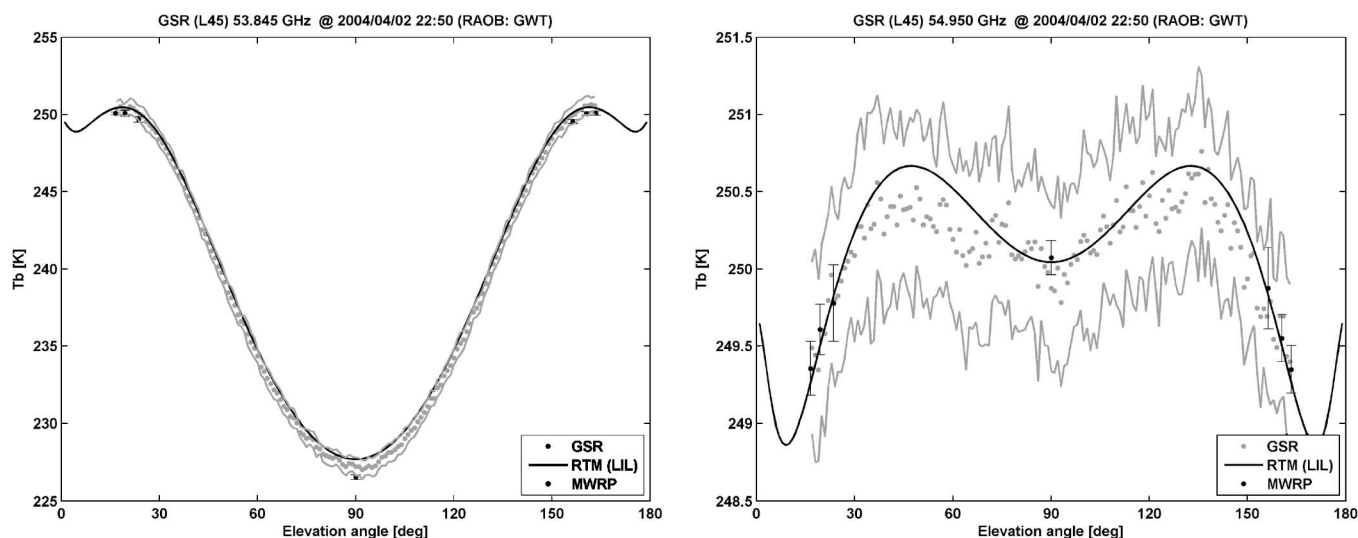
Fig. 10. Comparison of simulated and measured T_b during a series of elevation scans. Only the two GSR channels that overlap in frequency with two MWRP channels are shown. The black solid line indicates the simulations (absorption model in [21]) based on the RAOB launched on April 2, 2004 at 2300 UTC, and the gray and black dots represent simultaneous GSR and MWRP measurements. Standard deviation of MWRP and GSR measurements during the first 30 min of the balloon ascent are shown with black bars and gray solid line, respectively.
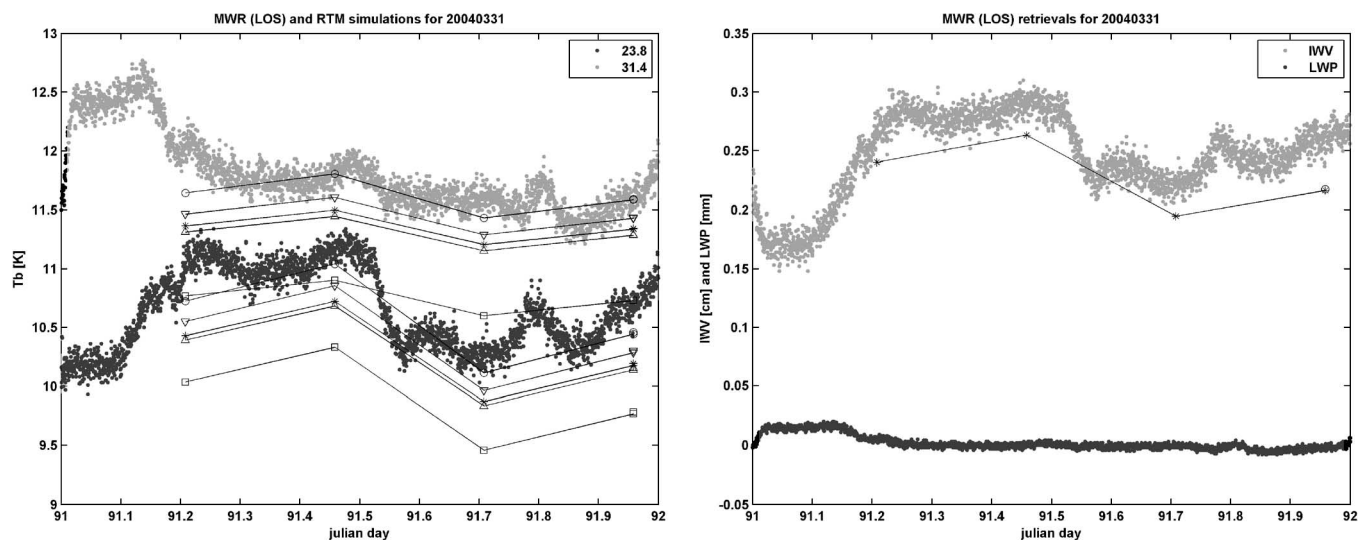

Fig. 11. (Left) MWR 23.8 and 31.4 T_b with RAOB simulations (symbols as in Fig. 9). (Right) MWR-retrieved IWV and LWP with radiosonde-derived IWV (black line). The sharp drop in IWV at around 91.5 jd was used for quantitative estimate of the sensitivity of GSR, MWR, and MWRP channels to changes in low water vapor contents.

of absorption models. Because a comprehensive analysis is beyond the scope of this paper, here, we want to show just two GSR channels (53.845 and 54.95 GHz), selected for their frequency overlap with two channels (53.85 and 54.94 GHz) operating on the MWRP. Thus, in Fig. 10, we compare T_b simulated from a RAOB with GSR and MWRP measurements at these two pairs of channels in the range of elevation angles scanned during the experiment. It is evident that measurements and simulations all agree within the total uncertainty. Note that the GSR scan provides a wealth of information compared to the MWRP, whose scan is limited to three dwell positions per side. Not considering angles lower than 3.5 air masses, where the effect of sidelobes might become important, the GSR continuous in-angle scanning provides as much information as the one

simulated from the RAOB profiles. In other words, each GSR channel provides the maximum angular information content obtainable by a single ground-based radiometric channel.

The spectrum of atmospheric opacity in Fig. 3 shows that there are at least two orders of magnitude between absorption in the 22-GHz water-vapor line and higher frequency lines, as 183 and 380 GHz. Therefore, in the dry Arctic conditions, we do expect small variations in IWV to cause much larger response at 183 and 380 GHz than at 20–30 GHz. In Fig. 11, we show T_b at 23.8 and 31.4 GHz as measured by the ARM dual-channel MWR for the same day considered in Fig. 9. In addition, we show the IWV and LWP operational retrievals, obtained by ARM, processing the MWR T_b with statistical regression [31]. Note that a GPS receiver was also located at

the same site. IWV from GPS and MWR agreed within 0.03 cm over the WVIOP2004 period, although GPS data were affected by a substantial scatter, mostly associated with multipath propagation due to low satellite orbits and high surface reflectivity [4] and, thus, are not shown in Fig. 11. As observed by the MWR, during the 24 h in Fig. 11, IWV ranges from 0.15 to 0.30 cm, with an average value and a total variation of 0.22 and 0.15 cm, respectively. For the same 24 h, the total variation of T_b does not exceed 1.5 K for both MWR channels. On the other hand, the total variation of T_b at millimeter- and submillimeter-wave channels can be as high as 40 K, as shown in Fig. 9. In particular, let us consider the sharp IWV drop of about 0.07 cm that occurred around 91.5 Julian day (jd). This IWV drop causes T_b at 23 GHz to decrease about 0.9 K, while at 183 ± 7, 340, and 380 ± 17 GHz, T_b decrease about 27, 31, and 36 K, respectively. By simply dividing the variation in T_b by the variation in IWV, we can give a rough estimate of the sensitivity of these channels to small changes in IWV. Using these data, we find 12.8, 385, 442, and 514 K/cm for 23, 183 ± 7, 340, and 380 ± 17 GHz, respectively, which agree with simulations reported in the study in [23]. However, as discussed in the study in [23], millimeter- and submillimeter-wave channels show a nonlinear response for higher values of IWV. Thus, these sensitivity estimates are intended only for the range of linearity, which differs from one channel to the other depending upon the corresponding opacity.

VI. DISCUSSION

The GSR data presented in Figs. 8–10 were obtained with the calibration procedure described in Section IV-B and Appendix I-A–D. Since the GSR is a research unit and further hardware characterization is ongoing, future upgrades to the calibration procedure may be made in order to achieve the best possible accuracy with this instrument. Nevertheless, a few results are worth discussing.

As expected, Fig. 8 shows that all of the GSR channels are suitable for atmospheric observations in the cold dry Arctic environment. The fact that, in those atmospheric conditions, very sensitive channels such as 183 ± 0.5, 183 ± 1, and 380 ± 4 GHz are not saturated makes them very appealing for the accurate retrieval of very low water vapor content in the Arctic. On the other hand, window channels, such as 89 and 340 GHz, have great potential for the accurate retrieval of low LWP. Moreover, the dual-polarization gives an opportunity to study the depolarization ratio caused by ice particles forming ice and mixed-phase clouds. The characteristic of observing both angular and spectral signatures is very important, as they provide information on the atmospheric thermodynamic state. The ability to retrieve temperature and humidity profiles from ground-based multichannel and multiangle observations is described in the study in [31] by means of the incremental weighting functions for 20–60-GHz channels and was later extended in frequency up to 190 GHz by Racette *et al.* [23] and to GSR channels by Cimini *et al.* [4] and [5]. Furthermore, the information content of the continuous elevation scans provides a new prospect for the study of absorption models because of the large dynamic range we span with each frequency.

The time series of zenith T_b presented in Fig. 9 are very promising. All the water-vapor channels are highly correlated and show large sensitivity to change in water-vapor content. As an example, the 0.07-cm drop in IWV estimated by the dual-channel MWR (Fig. 11) is detected by some GSR water-vapor channels as a change in T_b of more than 20 K. In the 20–30-GHz band, operationally used by ARM to retrieve water-vapor content, the same IWV drop corresponds to a T_b change of less than 1 K. Thus, some GSR channels were shown to be more than 20 times more sensitive to small changes in IWV than the conventional instruments used by ARM. Of course, we need to consider that calibration uncertainties are smaller for 20–30 GHz than for 183–380-GHz channels. Nevertheless, even considering 0.3-K error at 23.8 GHz and 3 K in the 183–380-GHz region, the corresponding error in retrieved IWV would be three to six times smaller using 183–380 GHz instead of 20–30-GHz channels [23]. It is worth mentioning that millimeter and submillimeter wavelengths may be affected by non-negligible scattering by hydrometers during cloudy conditions. Thus, scattering contributions and nonlinear T_b response could potentially affect the retrieval performances, if not properly handled. A detailed discussion of these effects is given in the study in [5].

VII. SUMMARY, CONCLUSION, AND FUTURE WORK

This paper describes the calibration and the first deployment of a new instrument, the GSR. The GSR was designed, developed, and deployed by the Microwave System Development Branch of NOAA/PSD, using an original architecture that allows for continuous whole-sky accurate observations. The principal advantages of the GSR are its effective calibration procedure and the rich information provided.

The GSR calibration procedure consists of three stages that rely on internal references, external targets, and sky symmetry, which corresponds to three techniques commonly used for ground-based radiometers. The three stages together are demonstrated to provide a high level of accuracy under both clear and cloudy skies. This is extremely important for the study of Arctic cloud properties, because the accuracy of instruments without this feature becomes questionable under prolonged cloudy periods.

The GSR data provide unprecedented information. The sky is observed simultaneously at 25 microwave and one infrared channels during continuous elevation scanning. The channels were selected for the retrieval of atmospheric temperature and humidity profiles, integrated content of vapor and liquid water, and cloud-depolarization ratio. In particular, 12 submillimeter-wave channels were specially chosen for the retrieval of very low content of water vapor and liquid, conditions typical of the Arctic winter. The atmospheric scans are performed continuously at angles from $16°$ to $165°$ in elevation, stopping at dwell positions corresponding to multiples of the atmospheric air mass. The GSR was deployed for the first time during the Arctic Winter Radiometric Experiment 2004, collecting atmospheric scans under a large variety of conditions. Selected results were discussed, confirming expectations about the GSR performances.

The large spectral and angular information provided by the GSR provides a new perspective in ground-based microwave remote sensing. The use of GSR data for the retrieval of atmospheric properties is currently in progress [4], [5]. Our future research will be focused on the study of atmospheric absorption models, the development of retrieval techniques with millimeter and submillimeter waves, and finally, the comparison and the integration of GSR data with measurements from other remote-sensing instruments.

APPENDIX I
CALIBRATION EQUATIONS

A. Internal Calibration

In the case of electronically switched radiometers (55 and 89 GHz), the radiance available from the internal references is computed by using the nominal values for the attenuation of the noise attenuator (NA) and for the equivalent noise ratio (ENR) of the diode noise generator (NG). For the mechanically switched radiometers (183, 340, and 380 GHz), the radiance emitted by the blackbody targets (bb) is computed using the Planck function $B_\nu(T) = (2h\nu^3/c^2)[1/(e^{h\nu/kT} - 1)]$ (where h is the Planck's constant, k is the Boltzmann's constant, c is the speed of light, and ν is the frequency) evaluated at their physical temperature, assuming unit emissivity. Therefore, the radiances used in the internal calibration are

$$B_{\nu,C}^{\mathrm{INT}} = \begin{cases} B_\nu(T_{\mathrm{NA}}), & \text{for 55 and 89 GHz} \\ B_\nu(T_{bb,C}), & \text{for 183, 340, and 380 GHz} \end{cases} \quad (1)$$

and

$$B_{\nu,H}^{\mathrm{INT}} = \begin{cases} B_\nu(T_{\mathrm{ON}})\alpha \\ \quad + B_\nu(T_{\mathrm{NA}})(1-\alpha), & \text{for 55 and 89 GHz} \\ B_\nu(T_{bb,H}), & \text{for 183, 340,} \\ & \text{and 380 GHz} \end{cases} \quad (2)$$

$$B_\nu(T_{\mathrm{ON}}) = B_\nu(T_0)(1 + 10^{\mathrm{ENR}/10}) \quad (3)$$

$$\mathrm{ENR} = \mathrm{ENR}(T_0) + \beta(T_{\mathrm{NG}} - T_0) \quad (4)$$

where T_{NA}, T_{NG}, $T_{bb,C}$, and $T_{bb,H}$ are the physical temperatures of NA, NG, cold bb, and hot bb, respectively, T_{ON} is the equivalent brightness temperature of the injected noise, α is the nominal value of NA attenuation (-24.6 dB for 55 GHz and -18.6 dB for 89 GHz), $\mathrm{ENR}(T_0)$ is the ENR at the reference temperature $T_0 = 290$ K (23 dB for 55 GHz and 17 dB for 89 GHz), while β is the correction coefficient (0.03 dB/K) that accounts for thermal drift in the ENR. The values of $T_{bb,C}$ and $T_{bb,H}$ come from an average of the temperatures measured by two thermistors mounted close to the center and to the edge of each target. The output voltage (V) detected by the radiometers at each separated channel is then converted into radiance via the following:

$$B_\nu^{\mathrm{INT}} = (V - O^{\mathrm{INT}})/G^{\mathrm{INT}} \quad (5)$$

$$G^{\mathrm{INT}} = (V_{H_{\mathrm{INT}}} - V_{C_{\mathrm{INT}}})/(B_{\nu,H}^{\mathrm{INT}} - B_{\nu,C}^{\mathrm{INT}}) \quad (6)$$

$$O^{\mathrm{INT}} = (V_{C_{\mathrm{INT}}} B_{\nu,H}^{\mathrm{INT}} - V_{H_{\mathrm{INT}}} B_{\nu,C}^{\mathrm{INT}})/(B_{\nu,H}^{\mathrm{INT}} - B_{\nu,C}^{\mathrm{INT}}) \quad (7)$$

where $V_{C_{\mathrm{INT}}}$ and $V_{H_{\mathrm{INT}}}$ are the detected voltages during the observation of internal cold and hot references, respectively,

while G^{INT} and O^{INT} represent the internal (from the input switch to the output) gain and the offset and have the units of $\mathrm{V} \cdot \mathrm{m}^2 \cdot \mathrm{sr} \cdot \mathrm{Hz/W}$ and V, respectively.

Due to nonideal hardware when the radiometers inputs are switched to the internal references, there is leakage from the signal coming from the antenna. Considering in first approximating the switch as a lossless nonreflecting triport device (i.e., the S-parameter coefficients are reduced to $|S_{2,3}|^2 = 1 - |S_{2,1}|^2 = \lambda$), when the radiometers are looking to the internal references, we have

$$\begin{aligned} V_{H_{\mathrm{INT}}} &= \hat{G}^{\mathrm{INT}} \left(B_{\nu,H}^{\mathrm{INT}} |S_{2,3}|^2 + B_{\nu,S}^{\mathrm{INT}} |S_{2,1}|^2\right) + \hat{O}^{\mathrm{INT}} \\ &= \hat{G}^{\mathrm{INT}} \left(B_{\nu,H}^{\mathrm{INT}} \lambda + B_{\nu,S}^{\mathrm{INT}} (1 - \lambda)\right) + \hat{O}^{\mathrm{INT}} \quad (8) \\ V_{C_{\mathrm{INT}}} &= \hat{G}^{\mathrm{INT}} \left(B_{\nu,C}^{\mathrm{INT}} |S_{2,3}|^2 + B_{\nu,S}^{\mathrm{INT}} |S_{2,1}|^2\right) + \hat{O}^{\mathrm{INT}} \\ &= \hat{G}^{\mathrm{INT}} \left(B_{\nu,C}^{\mathrm{INT}} \lambda + B_{\nu,S}^{\mathrm{INT}} (1 - \lambda)\right) + \hat{O}^{\mathrm{INT}} \quad (9) \end{aligned}$$

where $\hat{G}^{\mathrm{INT}}$ and $\hat{O}^{\mathrm{INT}}$ are the internal gain and offset that account for the leakage of the switch, and $B_{\nu,S}^{\mathrm{INT}}$ is the scene radiance, initially determined using (5). We remember that "scene" refers to both hot and cold external targets as well as to the atmosphere. As described in the study in [7], the leakage factor λ can be estimated from the output voltages. In fact, using the notation in which $V_{S_{\mathrm{INT}}}|_{H_{\mathrm{EXT}}}$ indicates the detected voltage when the radiometer input is switched to scene with the antenna looking at the external hot target and calling $B_{\nu,H_{\mathrm{EXT}}}^{\mathrm{INT}}$ as the internal calibrated radiance during this period, we have

$$\begin{aligned} \Delta V_H &= V_{H_{\mathrm{INT}}}|_{H_{\mathrm{EXT}}} - V_{H_{\mathrm{INT}}}|_{S_{\mathrm{EXT}}} \\ &= \hat{G}^{\mathrm{INT}} \left(B_{\nu,H_{\mathrm{EXT}}}^{\mathrm{INT}} - B_{\nu,S_{\mathrm{EXT}}}^{\mathrm{INT}}\right)(1 - \lambda) \quad (10) \\ \Delta V_S &= V_{S_{\mathrm{INT}}}|_{H_{\mathrm{EXT}}} - V_{S_{\mathrm{INT}}}|_{S_{\mathrm{EXT}}} \\ &= \hat{G}^{\mathrm{INT}} \left(B_{\nu,H_{\mathrm{EXT}}}^{\mathrm{INT}} - B_{\nu,S_{\mathrm{EXT}}}^{\mathrm{INT}}\right). \quad (11) \end{aligned}$$

Combining (10) and (11), it results that $\Delta V_H = (1 - \lambda)\Delta V_S$. Thus, we estimate the leakage factor λ for each channel by fitting a sample of realizations of ΔV_H and ΔV_S with a first-order polynomial.

Finally, inserting (8) and (9) in (6) and (7) and solving for $\hat{G}^{\mathrm{INT}}$ and $\hat{O}^{\mathrm{INT}}$, we obtain

$$\hat{G}^{\mathrm{INT}} = G^{\mathrm{INT}}/\lambda \quad (12)$$

$$\hat{O}^{\mathrm{INT}} = O^{\mathrm{INT}} - \frac{1 - \lambda}{\lambda} G^{\mathrm{INT}} B_{\nu,S}^{\mathrm{INT}} \quad (13)$$

and the leakage-corrected $B_{\nu,S}^{\mathrm{INT}}$ is finally

$$B_{\nu,S}^{\mathrm{INT}} = \left(V_S - \hat{O}^{\mathrm{INT}} - (1 - \lambda)\hat{G}^{\mathrm{INT}} B_{\nu,C}^{\mathrm{INT}}\right)/\lambda\hat{G}^{\mathrm{INT}} \quad (14)$$

from which we determine the scene brightness temperature $T_{b,S}^{\mathrm{INT}}$, solving the inverse of the Planck function

$$T_{b,S}^{\mathrm{INT}} = B_\nu^{-1}\left(B_{\nu,S}^{\mathrm{INT}}\right) = \frac{h\nu/k}{\log\left(1 + \frac{2h\nu^3/c^2}{B_{\nu,S}^{\mathrm{INT}}}\right)}.$$

B. External Calibration

The radiance calibrated with the internal references can be converted into absolute radiance via the following:

$$B_\nu^{\text{EXT}} = \left(B_\nu^{\text{INT}} - O^{\text{EXT}}\right)/G^{\text{EXT}} \quad (15)$$

$$G^{\text{EXT}} = \left(B_{\nu,H_{\text{EXT}}}^{\text{INT}} - B_{\nu,C_{\text{EXT}}}^{\text{INT}}\right)/\left(B_{\nu,H}^{\text{EXT}} - B_{\nu,C}^{\text{EXT}}\right) \quad (16)$$

$$O^{\text{EXT}} = \left(B_{\nu,C_{\text{EXT}}}^{\text{INT}} B_{\nu,H}^{\text{EXT}} - B_{\nu,H_{\text{EXT}}}^{\text{INT}} B_{\nu,C}^{\text{EXT}}\right)/\left(B_{\nu,H}^{\text{EXT}} - B_{\nu,C}^{\text{EXT}}\right) \quad (17)$$

where $B_{\nu,C_{\text{EXT}}}^{\text{INT}}$ and $B_{\nu,H_{\text{EXT}}}^{\text{INT}}$ are the internal calibrated radiances during the observation of external cold and hot targets, respectively, while $B_{\nu,C}^{\text{EXT}}$ and $B_{\nu,H}^{\text{EXT}}$ are the radiances emerging from the external cold and hot target, respectively. The values of $B_{\nu,C}^{\text{EXT}}$ and $B_{\nu,H}^{\text{EXT}}$ are estimated from the physical temperature of the absorbers (T_C^{EXT} and T_H^{EXT}, measured by 12 thermistors distributed in the volume of each target's foam), the emissivity of the absorbers ($\hat{\varepsilon} = 0.995$) and the spill-over radiance $B_{\nu,A}$. This radiance results from emission by the components within the protecting cover, and thus, its value is estimated from the physical temperature inside the GSR housing. Hence

$$B_{\nu,H}^{\text{EXT}} = \hat{\varepsilon} B_\nu\left(T_H^{\text{EXT}}\right) + (1-\hat{\varepsilon})B_{\nu,A} \quad (18)$$

$$B_{\nu,C}^{\text{EXT}} = \hat{\varepsilon} B_\nu\left(T_C^{\text{EXT}}\right) + (1-\hat{\varepsilon})B_{\nu,A}. \quad (19)$$

Note that G^{EXT} is unitless, while O^{EXT} has the units of watts per square meter per Steradian per hertz [W/(m² · sr · Hz)]. The radiance calibrated with the external targets can be expressed with the respect to the original voltage as the following:

$$B_\nu^{\text{EXT}} = \left(B_\nu^{\text{INT}} - O^{\text{EXT}}\right)/G^{\text{EXT}}$$

$$= \frac{(V - \hat{O}^{\text{INT}})/\hat{G}^{\text{INT}} - O^{\text{EXT}}}{G^{\text{EXT}}}$$

$$= \frac{V - \hat{O}^{\text{INT}} - \hat{G}^{\text{INT}} O^{\text{EXT}}}{\hat{G}^{\text{INT}} G^{\text{EXT}}}$$

$$= (V - O^{\text{INT+EXT}})/G^{\text{INT+EXT}} \quad (20)$$

$$G^{\text{INT+EXT}} = \hat{G}^{\text{INT}} G^{\text{EXT}} \quad (21)$$

$$O^{\text{INT+EXT}} = \hat{O}^{\text{INT}} + \hat{G}^{\text{INT}} O^{\text{EXT}} \quad (22)$$

where $G^{\text{INT+EXT}}$ and $O^{\text{INT+EXT}}$ have the units of volts per square meter per Steradian per hertz [(V · m² · sr · Hz)/W] and volts (V), respectively.

C. Tipping-Curve Calibration

In the case of GSR, we choose the emissivity of the external targets as the compound factor to be tuned with the tip-curve method. From (16) and (17), we extract the following:

$$G^0 = \left(B_{\nu,H_{\text{EXT}}}^{\text{INT}} - B_{\nu,C_{\text{EXT}}}^{\text{INT}}\right) / \left(B_\nu\left(T_H^{\text{EXT}}\right) - B_\nu\left(T_C^{\text{EXT}}\right)\right) \quad (23)$$

$$O^0 = \left(B_{\nu,C_{\text{EXT}}}^{\text{INT}} B_\nu\left(T_H^{\text{EXT}}\right) - B_{\nu,H_{\text{EXT}}}^{\text{INT}} B_\nu\left(T_C^{\text{EXT}}\right)\right)$$
$$/ \left(B_\nu\left(T_H^{\text{EXT}}\right) - B_\nu\left(T_C^{\text{EXT}}\right)\right) \quad (24)$$

such that

$$G^{\text{EXT}} = G^0/\hat{\varepsilon} \quad (25)$$

$$O^{\text{EXT}} = O^0 - G^0\frac{1-\hat{\varepsilon}}{\hat{\varepsilon}}B_{\nu,A}. \quad (26)$$

Note that (23) and (24) would correspond to the external gain and offset assuming perfect unitary emissivity. Thus, the radiance calibrated with the external targets can be expressed as

$$B_\nu^{\text{EXT}} = \left(B_\nu^{\text{INT}} - O^0 + \frac{1-\hat{\varepsilon}}{\hat{\varepsilon}}G^0 B_{\nu,A}\right)/(G^0/\hat{\varepsilon})$$

$$= \hat{\varepsilon}\left(\frac{B_\nu^{\text{INT}} - O^0}{G^0} - B_{\nu,A}\right) + B_{\nu,A}. \quad (27)$$

This represents the estimate of the radiance with the assumption of a constant target emissivity. The tipping-curve method is then used to refine this assumption by introducing a correction factor r that accounts for departures of the GSR system from our ideal model. Thus, (27) becomes

$$B_\nu^{\text{TIP}}(r) = r\hat{\varepsilon}\left(\frac{B_\nu^{\text{INT}} - O^0}{G^0} - B_{\nu,A}\right) + B_{\nu,A}$$

$$= r\left[\hat{\varepsilon}\left(\frac{B_\nu^{\text{INT}} - O^0}{G^0} - B_{\nu,A}\right) + B_{\nu,A} - B_{\nu,A}\right] + B_{\nu,A}$$

$$= r\left(B_\nu^{\text{EXT}} - B_{\nu,A}\right) + B_{\nu,A} \quad (28)$$

which leads to the equation we use with the tip-curve method to determine the factor r

$$B_\nu^{\text{TIP}}(r) = r\left(B_\nu^{\text{EXT}} - B_{\nu,A}\right) + B_{\nu,A}. \quad (29)$$

Following [14], we introduce the mean radiating temperature T_{mr}, the atmospheric opacity τ, and the air mass a (all functions of the elevation angle ϑ_i) as

$$B_\nu\left(T_{mr}(\vartheta_i)\right) = B_\nu(T_{mr,i}) = \frac{\int_0^\infty B_\nu(T)e^{-\tau(\vartheta_i)}d\tau(\vartheta_i)}{\left(1 - e^{-\tau(\vartheta_i,\infty)}\right)} \quad (30)$$

$$\tau(\vartheta_i, r) = \ln\left(\frac{B_\nu(T_{mr,i}) - B_\nu(T_{bg})}{B_\nu(T_{mr,i}) - B_\nu^{\text{TIP}}(r)}\right) = \tau_i(r) \quad (31)$$

$$a(\vartheta_i) = \tau(\vartheta_i)/\tau(\vartheta_z) = 1/\sin(\vartheta_i) = a_i,$$
$$\text{where } \vartheta_z = 90^0 \text{ (i.e., zenith)}. \quad (32)$$

We determine the factor r by solving the following least square problem:

$$Q(r) = \frac{1}{N}\sum_{i=1}^N \left(t_i(r) - \bar{t}(r)\right)^2 \quad (33)$$

where

$$t_i(r) = \tau_i(r)/a_i \quad \bar{t}(r) = \frac{1}{N}\sum_{i=1}^N t_i(r). \quad (34)$$

Minimization with respect to r yields

$$F(r) = \sum_{i=1}^{N} (t_i - \bar{t})(z_i - \bar{z}) = 0 \qquad (35)$$

where

$$z_i = \frac{1}{a_i \left(B_\nu(T_{mr,i}) - B_{\nu,i}^{\mathrm{TIP}}(r)\right)} \frac{\partial B_{\nu,i}^{\mathrm{TIP}}(r)}{\partial r}$$

$$= \frac{B_{\nu,i}^{\mathrm{EXT}} - B_{\nu,A}}{a_i \left(B_\nu(T_{mr,i}) - B_{\nu,i}^{\mathrm{TIP}}(r)\right)}$$

$$\bar{z}(r) = \frac{1}{N} \sum_{i=1}^{N} z_i(r). \qquad (36)$$

Finding the zero of $F(r)$ is a well-posed problem, as shown in the study in [14]. Thus, the gain $[(\mathrm{V} \cdot \mathrm{m}^2 \cdot \mathrm{sr} \cdot \mathrm{Hz})/\mathrm{W}]$ and offset (V) as corrected for the target emissivity are

$$G^{\mathrm{EXT+TIP}} = G^0 / r\hat{\varepsilon} = G^{\mathrm{EXT}} / r \qquad (37)$$

$$O^{\mathrm{EXT+TIP}} = O^0 - G^0 \frac{1 - r\hat{\varepsilon}}{r\hat{\varepsilon}} B_{\nu,A}$$

$$= O^{\mathrm{EXT}} - G^{\mathrm{EXT}} \frac{1 - r}{r} B_{\nu,A}. \qquad (38)$$

D. Overall Calibration

Considering (21), (22), (37), and (38), the three steps of calibration can be combined and applied all at once by using the following equations:

$$B_\nu^{\mathrm{TIP}} = (V - O^{\mathrm{TOT}}) / G^{\mathrm{TOT}} \qquad (39)$$

$$G^{\mathrm{TOT}} = \hat{G}^{\mathrm{INT}} G^{\mathrm{EXT+TIP}}$$

$$= \hat{G}^{\mathrm{INT}} G^{\mathrm{EXT}} / r = G^{\mathrm{INT+EXT}} / r \qquad (40)$$

$$O^{\mathrm{TOT}} = \hat{O}^{\mathrm{INT}} + \hat{G}^{\mathrm{INT}} O^{\mathrm{EXT+TIP}}$$

$$= \hat{O}^{\mathrm{INT}} + \hat{G}^{\mathrm{INT}} \left(O^{\mathrm{EXT}} - G^{\mathrm{EXT}} \frac{1 - r}{r} B_{\nu,A}\right)$$

$$= O^{\mathrm{INT+EXT}} - G^{\mathrm{INT+EXT}} \frac{1 - r}{r} B_{\nu,A} \qquad (41)$$

where G^{TOT} and O^{TOT} have the units of $(\mathrm{V} \cdot \mathrm{m}^2 \cdot \mathrm{sr} \cdot \mathrm{Hz})/\mathrm{W}$ and V, respectively. Finally, this calibrated radiance is converted into brightness temperature T_b^{TIP}, solving the inverse of the Planck function

$$T_b^{\mathrm{TIP}} = B_\nu^{-1}\left(B_\nu^{\mathrm{TIP}}\right) = \frac{h\nu/k}{\log\left(1 + \frac{2h\nu^3/c^2}{B_\nu^{\mathrm{TIP}}}\right)}. \qquad (42)$$

ACKNOWLEDGMENT

REFERENCES

[1] D. W. Allan, "Statistics of atomic frequency standards," *Proc. IEEE*, vol. 54, no. 2, pp. 221–230, Feb. 1966.

[2] S. A. Boukabara, S. A. Clough, J.-L. Moncet, A. F. Krupnov, M. Tretyakov, and V. V. Parshin, "Uncertainties in the temperature dependence of the line coupling parameters of the microwave Oxygen band: Impact study," *IEEE Trans. Geosci. Remote Sens.*, vol. 43, no. 5, pp. 1109–1114, May 2005.

[3] D. Cimini, E. R. Westwater, Y. Han, and S. J. Keihm, "Ground-based microwave radiometer measurements and radiosondes comparisons during the WVIOP2000 field experiment," *IEEE Trans. Geosci. Remote Sens.*, vol. 41, no. 11, pp. 2605–2615, Nov. 2003.

[4] D. Cimini, E. R. Westwater, A. J. Gasiewski, M. Klein, V. Leuski, V. Mattioli, S. Dowlatshahi, and J. Liljegren, "Ground-based millimeter- and submillimeter-wave observations of the arctic atmosphere," in *Proc. Spec. Meeting Microrad*, Mar. 2006, pp. 247–251.

[5] D. Cimini, E. R. Westwater, A. J. Gasiewski, M. Klein, V. Leuski, and J. Liljegren, "Ground-based millimeter- and submillimeter-wave observations of low vapor and liquid water contents," *IEEE Trans. Geosci. Remote Sens.*, vol. 45, no. 7, pp. 2169–2180, Jul. 2007.

[6] I. Corbella, A. J. Gasiewski, M. Klein, and J. R. Piepmeier, "Compensation of elevation angle variations in polarimetric brightness temperature measurements from airborne microwave radiometers," *IEEE Trans. Geosci. Remote Sens.*, vol. 39, no. 1, pp. 193–195, Jan. 2001.

[7] I. Corbella, A. J. Gasiewski, M. Klein, V. Leuski, A. J. Francavilla, and J. R. Piepmeier, "On-board accurate calibration of dual-channel radiometers using internal and external references," *IEEE Trans. Microw. Theory Tech.*, vol. 50, no. 7, pp. 1816–1820, Jul. 2002.

[8] J. A. Curry, W. B. Rossow, D. Randall, and J. L. Schramm, "Overview of Arctic cloud and radiation characteristics," *J. Climate*, vol. 9, no. 8, pp. 1721–1764, Aug. 1996.

[9] R. H. Dicke, "The measurement of thermal radiation at microwave frequencies," *Rev. Sci. Instrum.*, vol. 17, no. 7, pp. 268–279, Jul. 1946.

[10] S. G. Dowlatshahi, "A 340 GHz scanning radiometer for sensing clouds in the Arctic environment," M.S. thesis, Faculty Graduate School, Dept. Electr. and Comput. Eng., Univ. Colorado, Boulder, CO, 2004.

[11] A. J. Gasiewski, J. R. Piepmeier, R. E. McIntosh, C. T. Swift, J. R. Carswell, W. J. Donnelly, E. Knapp, E. R. Westwater, V. I. Irisov, L. S. Fedor, and D. C. Vandemark, "Combined high-resolution active and passive imaging of ocean surface winds from aircraft," in *Proc. Int. Geosci. Remote Sens. Symp.*, Singapore, Aug. 3–8, 1997, pp. 1001–1005.

[12] P. F. Goldsmith and E. L. Moore, "Gaussian optics lens antennas," *Microw. J.*, vol. 27, no. 7, pp. 153–157, Jul. 1984.

[13] J. P. Hach, "A very sensitive airborne microwave radiometer using two reference temperatures," *IEEE Trans. Microw. Theory Tech.*, vol. MTT-16, no. 9, pp. 629–636, Sep. 1968.

[14] Y. Han and E. R. Westwater, "Analysis and improvement of tipping calibration for ground-based microwave radiometers," *IEEE Trans. Geosci. Remote Sens.*, vol. 38, no. 3, pp. 1260–1277, May 2000.

[15] T. J. Hewison, "Aircraft validation of clear air absorption models at millimeter wavelengths (89–183 GHz)," *J. Geophys. Res.*, vol. 111, no. D14, D14 303, 2006.

[16] M. A. Janssen, "An introduction to the passive microwave remote sensing of atmospheres," in *Atmospheric Remote Sensing by Microwave Radiometry*, M. Janssen, Ed. New York: Wiley, 1993.

[17] E. R. Westwater, M. Klein, V. Leuski, A. J. Gasiewski, T. Uttal, D. A. Hazen, D. Cimini, V. Mattioli, B. L. Weber, S. Dowlatshahi, J. A. Shaw, J. S. Liljegren, B. M. Lesht, B. D. Zak, "The 2004 North Slope of Alaska Arctic Winter Radiometric Experiment" in *Proc. of 14th ARM Sci. Team Meeting*, Mar 22–26 2004, [Online].Available: http://www.arm.gov/publications/proceedings/conf14/extended_abs/westwater-er.pdf

[18] H. J. Liebe, "MPM, An atmospheric millimeter wave propagation model," *Int. J. Infrared Millim. Waves*, vol. 10, no. 6, pp. 631–650, 1989.

[19] H. J. Liebe, G. A. Hufford, and M. G. Cotton, "Propagation modeling of moist air and suspended water/ice particles at frequencies below 1000," in *Proc. AGARD Conf. 542, Atmospheric Propag. Effects Through Natural and Man-Made Obscurants Visible Through MM-Wave Radiation*, 1993, pp. 3.1–3.10.

[20] J. C. Liljegren, "Automatic self-calibration of ARM microwave radiometers," in *Microwave Radiometry and Remote Sensing of the Earth's Surface and Atmosphere*, P. Pampaloni and S. Paloscia, Eds. Utrecht, The Netherlands: VSP, 2000, pp. 433–443.

[21] J. C. Liljegren, S. A. Boukabara, K. Cady-Pereiria, and S. A. Clough, "The effect of the half-width of the 22-GHz water vapor line on retrievals of temperature and water vapor profiles with a 12-channel

microwave radiometer," *IEEE Trans. Geosci. Remote Sens.*, vol. 43, no. 5, pp. 1102–1108, May 2005.

[22] A. McGrath and T. Hewison, "Measuring the accuracy of MARSS—An airborne microwave radiometer," *J. Atmos. Ocean. Technol.*, vol. 18, no. 12, pp. 2003–2012, Dec. 2001.

[23] P. Racette, E. R. Westwater, Y. Han, A. Gasiewski, M. Klein, D. Cimini, W. Manning, E. Kim, J. Wang, and P. Kiedron, "Measuring low amounts of precipitable water vapor using millimeter-wave radiometry," *J. Atmos. Ocean. Technol.*, vol. 22, no. 4, pp. 317–337, Apr. 2005.

[24] J. Randa, A. E. Cox, D. K. Walker, M. Francis, J. Guerrieri, and K. MacReynolds, "Standard radiometers and targets for microwave remote sensing," in *Proc. Int. Geosci. Remote Sens. Symp.*, Anchorage, AK, 2004, p. 698.

[25] G. Rau, R. Schieder, and B. Vowinkel, "Characterization and measurement of radiometer stability," in *Proc. 14th Eur. Microw. Conf.*, Liege, Belgium, Sep. 10–13, 1984, pp. 248–253.

[26] A. Remmele. (2002). Precise calibration target for PSR/S ground based radiometer. NOAA ETL, Boulder, CO., CU/CET Tech. Rep., [Online]. Available: http://cet.colorado.edu/pubs/2002/Rem02/

[27] P. W. Rosenkranz, "Water vapor microwave continuum absorption: A comparison of measurements and models," *Radio Sci.*, vol. 33, no. 4, pp. 919–928, 1998.

[28] P. W. Rosenkranz, "Correction to 'Water vapor microwave continuum absorption: A comparison of measurements and models'," *Radio Sci.*, vol. 34, no. 4, p. 1025, 1999.

[29] K. Stamnes, R. G. Ellingson, J. A. Curry, J. E. Walsh, and B. D. Zak, "Review of science issues, deployment strategy, and status for the ARM North Slope of Alaska-adjacent Arctic Ocean climate research site," *J. Climate*, vol. 12, no. 1, pp. 46–63, 1999.

[30] F. T. Ulaby, R. K. Moore, and A. K. Fung, *Microwave Remote Sensing—Active and Passive*, vol. 1. Norwood, MA: Artech House, 1981.

[31] E. R. Westwater, "Ground-based microwave remote sensing of meteorological variables," in *Atmospheric Remote Sensing by Microwave Radiometry*, M. Janssen, Ed. Hoboken, NJ: Wiley, 1993, pp. 145–213.

[32] E. R. Westwater, P. E. Racette, and D. Cimini, "The arctic winter millimeter-wave radiometric experiment: Summary, conclusion and recommendations," in *Proc. 11th ARM Sci. Team Meeting*, Mar. 19–23, 2001. [Online]. Available: http://www.arm.gov/publications/proceedings/conf11/extended_abs/westwater_er.pdf

[33] E. R. Westwater, P. Racette, D. Cimini, and Y. Han, "Millimeter-wavelength forward-model radiative transfer comparisons based on ground-based observations taken during the 1999 North Slope of Alaska Radiometric Experiment," in *Proc. Int. Geosci. Remote Sens. Symp.*, Toulouse, France, Jul. 2003, vol. 2, pp. 1218–1221.

[34] E. R. Westwater, M. Klein, V. Leuski, A. J. Gasiewski, T. Uttal, D. A. Hazen, D. Cimini, V. Mattioli, B. L. Weber, S. Dowlatshahi, J. A. Shaw, J. S. Liljegren, B. M. Lesht, and B. D. Zak, "Initial results from the 2004 North Slope of Alaska Arctic Winter Radiometric Experiment," in *Proc. Int. Geosci. Remote Sens. Symp.*, Anchorage, AK, 2004, pp. 1374–1377.

[35] P. Zuidema, B. Baker, Y. Han, J. Intrieri, J. Key, P. Lawson, S. Matrosov, M. Shupe, R. Stone, and T. Uttal, "An Arctic springtime mixed-phase cloudy boundary layer observed during SHEBA," *J. Atmos. Sci.*, vol. 62, no. 1, pp. 160–176, Jul. 2004.

Domenico Cimini was born in Teramo, Italy, in 1973. He received the Laurea degree (*cum laude*) in physics and the Ph.D. degree from the University of L'Aquila, L'Aquila, Italy, in 1998 and 2002, respectively.

Since 1999, he has been collaborating with the Environmental Technology Laboratory, National Oceanic and Atmospheric Administration, Boulder, CO. In 2002, he was with the Center of Excellence CETEMPS, University of L'Aquila, working on radiometer calibration techniques, microwave radiative-transfer models, and ground- and satellite-based passive microwave and infrared radiometry. In 2004–2005, he was a Visiting Fellow at the Cooperative Institute for Research in Environmental Sciences, University of Colorado, Boulder. Then, he was with the Institute of Methodologies for the Environmental Analysis of the Italian National Research Council working on ground- and satellite-based observations of cloud properties. Since 2006, he has been an affiliate of the Center for Environmental Technology, Department of Electrical and Computer Engineering, University of Colorado, where he serves as Adjunct Professor.

Ed R. Westwater (SM'91–F'01) received the B.A. degree in physics and mathematics from the Western State College of Colorado, Gunnison, in 1959, and the M.S. and Ph.D. degrees in physics from the University of Colorado (CU), Boulder, in 1962 and 1970, respectively.

From 1960 to 1995, he was with the U.S. Department of Commerce. He has been with the Cooperative Institute for Research in Environmental Science (CIRES) since 1995. From 2000 to 2002, he was the Chairman of the U.S. National Committee for the International Union for Radio Science Commission F. He joined the NOAA-CU Center for Environmental Technology (CET) in 2006. He is currently a Research Professor with CET and CIRES, Department of Electrical and Computer Engineering, CU. He is the author or coauthor of more than 275 publications. From 1999 to 2002, he was an Associate Editor of *Radio Science*. His research interests are microwave absorption in the atmosphere, remote sensing of the atmosphere and ocean surface, microwave and infrared radiative transfer, ground- and satellite-based remote sensing by passive radiometry, and the application of mathematical inversion techniques to problems in remote sensing.

Dr. Westwater is a member of the American Meteorological Society, the American Geophysical Union, and the Mathematical Association of America He received the 15th V. Vaisala Award from the World Meteorological Society in 2001 and the Distinguished Achievement Award from the IEEE Geoscience and Remote Sensing Society in 2003. He was the Chairman and Organizer of the 1992 International Specialists Meeting on Microwave Radiometry and Remote Sensing Applications (MicroRad) and was a Co-organizer of the MicroRad 2001. He presented the American Meteorological Society's Remote Sensing Lecture in 1997. He is currently an Associate Editor of the IEEE TRANSACTIONS ON GEOSCIENCE AND REMOTE SENSING (TGARS) and served as a Guest Editor of the TGARS Special Issue devoted to MicroRad 2004 and of the TGARS Special Issue devoted to MicroRad 2006.

Albin J. Gasiewski (S'81–M'88–SM'95–F'02) received the B.S. degree in mathematics in 1983 and the B.S. and M.S. degrees in electrical engineering from Case Western Reserve University, Cleveland, OH, and the Ph.D. degree in electrical engineering and computer science from the Massachusetts Institute of Technology, Cambridge, in 1989.

From 1989 to 1997, he was a Faculty Member with the School of Electrical and Computer Engineering, Georgia Institute of Technology, where he became an Associate Professor. From 1997 to 2005, he was with the National Oceanic and Atmospheric Administration's Environmental Technology Laboratory (ETL), Boulder, CO, where he was the Chief of ETL's Microwave Systems Development Division. He is currently a Professor of electrical and computer engineering at the University of Colorado, Boulder, and the Director of the University of Colorado Center for Environmental Technology. He has developed and taught courses on electromagnetics, remote sensing, instrumentation, and wave-propagation theory. His technical interests include passive and active remote sensing, radiative transfer, antennas and microwave circuits, electronic instrumentation, meteorology, and oceanography.

Dr. Gasiewski is a Past President (2004–2005) of the IEEE Geoscience and Remote Sensing Society (GRSS). He is a member of the American Meteorological Society, American Geophysical Union, International Union of Radio Scientists (URSI), Tau Beta Pi, and Sigma Xi. He currently serves as Vice Chair of USNC/URSI Commission F. He served on the U.S. National Research Council's Committee on Radio Frequencies from 1989 to 1995. He was the General Cochair of IGARSS 2006, in Denver, CO, and was the recipient of the 2006 Outstanding Service Award from the GRSS.

Marian Klein (M'95) received the M.S. and Ph.D. degrees in electrical engineering from the Technical University of Košice, Letna, Slovak Republic, in 1986 and 1996, respectively.

From 1987 to 1996, he was a Faculty Member within the Faculty of Electrical Engineering and Informatics, Technical University of Košice. From September 1996 to June 1997, he was a Fulbright scholar at the Georgia Institute of Technology, working in the Laboratory for Radio Science and Remote Sensing. Since August 1998, he has been a Research Associate with the Cooperative Institute for Research in Environmental Sciences, University of Colorado, Boulder, and is the Laboratory Manager for the University of Colorado Center for Environmental Technology (CET). His areas of technical expertise include passive microwave remote sensing, radiative-transfer theory, and the development of millimeter- and submillimeter-wave instrument systems for environmental studies. He has an extensive knowledge and experience in radiometer system design for harsh environments—airborne or ground based. He successfully led many field deployments of radiometric systems used in many NASA, NOAA, DoE, and DoD experiments including several soil-moisture experiments (1999, 2002, 2003, and 2004), the Wakasa Bay Experiment (2003), the Cold Land Processes Experiments (2002 and 2003), and AMSR-E Arctic and Antarctic Sea-Ice Experiments (2003 and 2004). He was a Project Leader for the Ground-Based Scanning Radiometer deployed in Barrow, AK (2004). He is a Lead Field Engineer and Design and Fabrication Leader for several NOAA/Environmental Technology Laboratory (ETL) and CET instruments such as the Polarimetric Scanning Radiometer system including its PSR/A, PSR/CX, and PSR/S scanheads. In addition, he is currently the Chief Executive Officer of Boulder Environmental Sciences and Technology, LLC.

Vladimir Ye. Leuski received the degree in radio engineering from the Moscow Aviation Institute, Moscow, Russia, in 1971 and the Doctor's degree in radio physics from the Space Research Institute, Moscow, in 1984.

From 1974 to 1984, he was an Engineer and Senior Engineer at the Space Research Institute. From 1985 to 1990, he was with the Research Institute "Pulsar," Moscow, as the Chief of Laboratory. From 1991 to 1996, he worked at the Lebedev Physical Institute, Moscow. Since July 1996, he has been a Research Associate at the Cooperative Institute for Research in Environmental Sciences, University of Colorado, Boulder. His main scientific interests are the developmental of low-noise millimeter-wave components and radiometers and their application for remote sensing of the atmosphere and ocean surface.

Sally G. Dowlatshahi received the B.S. degree in electrical engineering from the University of Illinois, Chicago, in 2001, and the Master's degree in electrical engineering from the University of Colorado, Boulder, in 2004. Her Master's thesis focused on a 340-GHz radiometer development, deployment, and data processing and analysis.

She is currently working as a Systems Engineer at Northrop Grumman—Electronics Systems Sector in Boulder.